Astronomy & Astrophysics manuscript no. piirola
January 28, 2020

High precision polarimetry of nearby stars (d < 50 pc)

Mapping the interstellar dust and magnetic field inside the local bubble

V. Piirola[1,2] A. Berdyugin[1] P. C. Frisch[3] M. Kagitani[4] T. Sakanoi[4]
S. Berdyugina[5] A.A. Cole[6] C. Harlingten[6] and K. Hill[6]

[1] Department of Physics and Astronomy, University of Turku, Finland
e-mail: piirola@utu.fi, andber@utu.fi
[2] FINCA, University of Turku, FI-20014 Turku, Finland
[3] Department of Astronomy and Astrophysics, University of Chicago, Chicago IL 60637 USA
[4] Graduate School of Science, Tohoku University, Aoba-ku, Sendai 980-8578 Japan
[5] Leibniz-Institut für Sonnenphysik, D-79104 Freiburg, Germany
[6] Greenhill observatory, School of Natural Sciences, University of Tasmania, Private Bag 37, Hobart, TAS 7001 Australia

Received ; accepted

ABSTRACT

Context. To investigate the linear polarization produced by interstellar dust, aligned by the magnetic field in the solar neighborhood (d < 50 pc). Intrinsic effects from circumstellar processes are also searched from the polarization variability or wavelength dependence.
Aims. To detect and map dust clouds which give rise to statistically significant amounts of polarization in the starlight traversed through the cloud, and determine the interstellar magnetic field direction by the position angle of the observed polarization.
Methods. High precision broad-band (BVR) polarization observations are made of 361 stars in spectral classes F to G, with detection sensitivity at the level or better than 10^{-5} (0.001 percent). The sample consists of 125 stars in the magnitude range 6-9 observed at the 2.2 m UH88 telescope on Mauna Kea, 205 stars in the magnitude range 3-6 observed at the Japanese (Tohoku) T60 telescope on Haleakala, and 31 stars in the magnitude range 4-7 observed at the 1.27 m H127 telescope of the Greenhill Observatory, Tasmania. Identical copies of the Dipol-2 polarimeter are used on these three sites.
Results. Statistically significant (> 3σ) polarization is found in 115 stars, and > 2σ detection in 178 stars, out of the total sample of 361 stars. Polarization maps based on these data show filament-like patterns of polarization position angles, related to both the heliosphere geometry, the kinematics of nearby clouds, and the IBEX ribbon magnetic field. From long-term multiple observations a number (~ 20) of stars give evidence of intrinsic variability at the 10^{-5} level. This can be addressed to circumstellar effects (e.g. debris disks, chromospheric activity). The star HD 101805 shows a peculiar wavelength dependence, indicating size distribution of scattering particles different from that of a typical interstellar medium. Our high S/N measurements of nearby stars with very low polarization also provide a useful dataset for calibration purposes.

Key words. techniques: polarimetric – ISM: dust – ISM: magnetic fields – stars: activity – stars: circumstellar matter

1. Introduction

In the course of polarization studies of astrophysical objects which require very high S/N (see Berdyugin et al. 2016, 2018) we have observed samples of nearby stars (d < 50 pc) in order to determine and subtract the instrumental polarization produced by the telescope. This is achieved with a typical uncertainty of 2-3 x 10^{-6} (ppm) for each run, normally spanning over several days to one month intervals. To avoid intrinsic effects as much as possible, stars of spectral types F-G have been selected. These calibration measurements are crucial for each of the research program, but they also provide a valuable database about the minute amounts of polarization in each of the observed stars. The individual stellar data can in turn be used to map the interstellar magnetic field and dust content along the path the observed starlight has traversed.

While the interstellar magnetic field (ISMF) structure and dust content are relatively well understood from the polarization maps based on measurements of stars at larger distances, d > 50 pc up to the kpc ranges (see e.g. Berdyugin et al. 2014), the very low dust content and therefore small degrees of polarization within the local bubble have prevented detailed polarization studies until the recent development of extremely high S/N polarimeters, with 10^{-6} – 10^{-5} detection sensitivity (see e.g. Bailey et al. 2010, 2015; Piirola et al. 2014; Cotton et al. 2017, 2019).

Encouraged by the successful implementation of our high precision polarimeter (Dipol-2), and the availability of sufficient amounts of observing time from remotely operated telescopes at good observing sites, we have initiated a dedicated program for deriving the structure of the very local magnetic field from stellar polarization data. The need for a survey of optical polarizations that trace the local interstellar magnetic field became clear with the discovery by IBEX of an arc (or "ribbon") of energetic neutral atoms whose center traces the direction of the interstellar magnetic field shaping the heliosphere (McComas et al. 2009; Schwadron et al. 2009).

Target stars for this program were selected from objects in the Hipparcos catalog (Perryman et al. 1997). Channels devoid of nearby suitable target objects were found in the Hipparcos data in many locations, indicating either an irregular distribution of dust or an irregular distribution of suitable target stars. Some earlier results from our nearby star observations have been included in the studies by Frisch et al. (2015a,b), tracing the structure of the very local interstellar magnetic field.

In the present paper we give a detailed description of our current dataset and discuss the results based on the polarization map obtained. Statistical significance of the detections is addressed. It is also interesting to look for the evidence of intrinsic polarization variability in some of the stars observed. Examples are given of particular wavelength dependence found, suggesting effects from a circumstellar debris disk.

2. Observations

We have carried out observations in 2014-2019 at three telescopes, the 2.2 m UH88 telescope on Mauna Kea, the Tohoku 60 cm telescope (T60) on Haleakala, and the University of Tasmania (UTAS) 1.27 m (H127) telescope at Greenhill Observatory, Tasmania. Observations were made with the simultaneous three-color (*BVR*) polarimeter Dipol-2 (Piirola et al. 2014). Identical copies of the instrument are used at each of the three sites. At UH88 and T60 the observations were carried out in the remote operation mode. Some additional data on the stars in our sample were obtained at the NOT and WHT telescopes at ORM, La Palma, A summary of the observations is given in Table 1.

The polarimeter, Dipol-2, is capable of making simultaneous measurements in three passbands B, V, and R (see Figs. 1-2, and Table 2), with high sensitivity. The detection limit of polarization is at the level of 10^{-5}, set in practice by photon noise. An important asset of the instrument is that the sky background polarization is directly (optically) eliminated. The perpendicularly polarized components of sky are superimposed by the plane parallel calcite beam splitter, and sky polarization is thereby cancelled (Piirola 1973). This is essential, as the polarized flux from scattered skylight can exceed by orders of magnitude the signal from the target, particularly in bright Moon conditions. Dipol-2 has been found to be very stable and reliable instrument as demonstrated recently by detection of the variable polarization at 0.1 per cent level from the massive binaries HD 48099 (Berdyugin et al. 2016) and λ Tauri (Berdyugin et al. 2018).

The Dipol-2 polarimetry routine consists of cycles of 16 exposures at different orientations of the superachromatic half-wave retarder (22.5° steps), corresponding to a full (360°) rotation of the retarder. Each successive 4 exposures give one independent measurement of the normalized Stokes parameters $q = p\cos 2\theta$ and $u = p\sin 2\theta$, where p is the degree of linear polarization and θ the position angle of the maximum electric vector, in the equatorial frame of references. Accordingly, one cycle gives four independent measurements of q and u.

For the highest S/N measurements it is advantageous to strongly defocus images to spread light over a very large number of pixels. In this way we can expose up to 10^8 electrons in one stellar image without saturating the CCD pixels. Even if there are minor shifts in the position of the two perpendicularly polarized images of the target, vast majority of the pixels remain the same over the full measurement cycle (16 exposures). Minor imperfections in the flat field are eliminated in the reductions, since the ratio of the o- and e- beam transmission and efficiency, if constant, is automatically cancelled in the reduction algorithm. This provides inherently very stable instrument and detection sensitivity better than 10^{-5} (< 10 ppm) in ∼ 1 hour for sufficiently bright stars. In fact, Dipol-2 polarimeter is photon noise limited down to these very low polarization signal levels.

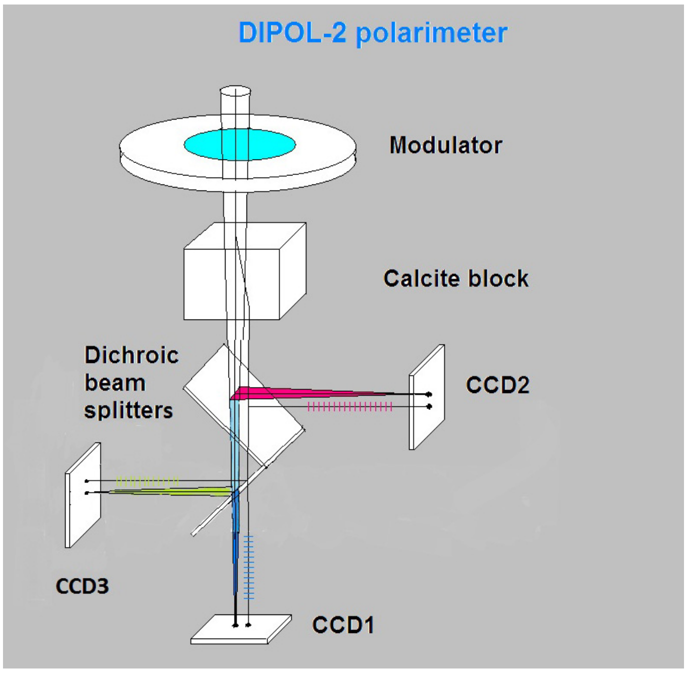

Fig. 1. The scheme of the Dipol-2 polarimeter. Rotatable superachromatic $\lambda/2$ retarder plate modulates the relative intensities of the two polarized beams produced by the calcite crystal, with an amount proportional to the degree of linear polarization of the incoming radiation. Two dichroic mirrors split the light into three passbands: blue, visible, and red. The fluxes of the two polarized stellar images in each band are measured with three highly sensitive cooled CCD detectors.

In order to beat down the photon noise to the required (10^{-5}) level, the total telescope time used for each star's nightly observation was 0.5-1.5 hours, depending on the brighness of the star. With a typical single exposure time of 1-3 sec, the total number of individual observations of the normalized Stokes parameters q and u for one star was usually in the range 128-256. This provides very good statistical error estimates for the nightly average points of q and u for each star.

Standard CCD reduction procedures (bias and dark subtraction, flat fielding) were applied prior to extracting the fluxes from the double images of the target, formed onto the CCD by the polarizing calcite beam splitter. Special centering algorithm and subframing procedures were used to facilitate processing a large number, up to several hundred, of exposures at the same time. In computing the mean values of q and u we applied a "2σ" iterative weighting algorithm. The initial mean and standard deviation were obtained applying equal weights to all points. Then on each step individual points deviating more than two standard deviations from the mean ($d > 2\sigma$) were given a lower weight, proportional to the inverse square of the error estimate, e_x. The value $e_x = \sigma$ for $d < 2\sigma$ was assumed to increase linearly from $e_x = 1\sigma$ to 3σ with d increasing from 2σ to 3σ. Points with $d > 3\sigma$ were rejected. The procedure converges fast and values of mean and standard deviation are obtained within a few iterations. Under normal conditions, 6–8 per cent of individual points deviated more than 2σ and were given lower weight ($W < 1$). The remaining 92–94 per cent of points were equally weighted ($W = 1$). The weighting procedure helps to suppress effects from transient clouds, moments of bad seeing, cosmic ray events, etc.

The simultaneous polarization measurements in the three (*BVR*) passbands provided by Dipol-2 are very useful for studying the wavelength dependence of polarization. Obviously, they

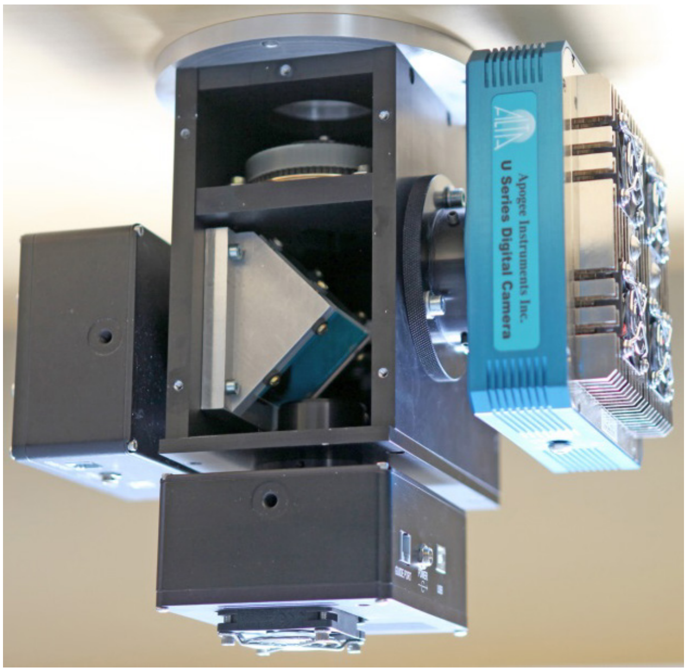

Fig. 2. Dipol-2 polarimeter with the front cover removed, showing (from top) the polarization modulator unit (retarder plate and the calcite plate), the dichroics unit dividing the light onto three CCDs: the blue (right), the visible (bottom), and the red (left).

Table 1. Summary of observations.

Telescope	JD Interval	Stars	mag range
UH88	2456818-7678	125	6.1 – 9.1
T60	2456994-8508	205	3.9 – 6.5
H127	2457775-8183	31	4.1 – 6.9
	Additional data:		
WHT	2457206-7407	12	7.2 – 8.4
NOT	2458687-8688	15	3.8 – 5.8

Table 2. Equivalent wavelengths and full widths at half maximum (FWHM) of the Dipol-2 passbands

Passband	λ_{eq}(nm)	FWHM (nm)
B	450	110
V	545	89
R	655	120

also improve the efficiency. There is only little internal absorption in the dichroic beam splitters used to separate the colour passbands.

In the case of the extremely low polarization values found in the stars inside the local bubble, the S/N in each of the wavelength bands (*BVR*) may not be sufficient to obtain useful data for constraining the wavelength dependence of interstellar polarization, and thereby the aligned grain size distribution. In such cases, and because of the relatively flat shape of the IS polarization curve in the optical part of the spectrum, it is meaningful to compute 'broad-band' (400-800 nm) polarization values by weighted averaging of the normalized Stokes parameters q and u obtained in the B, V, and R passbands, to improve the S/N and the statistical significance of the detection for very weak polarization signals.

3. Results and Discussion

3.1. Instrumental polarization

Because of the very small degree of polarization produced by the interstellar dust in the Solar vicinity, it is crucial to determine and subtract the effects of the telescope optics and the instrument itself from the measured polarization. This is done by observing nearby stars which can be assumed to be practically 'unpolarized', thanks to their proximity to us, and freedom of intrinsic polarization effects ensured by the selection of the spectral type (F-G main sequence stars).

However, we cannot assume that any single star has zero polarization within the strict limits required for the present work. Therefore, we always observe a sample of at least 15-20 stars in different parts of the sky and determine the instrumental polarization as the average of the q and u from the sample. In this way small effects of interstellar polarization in each of the observed stars tend to cancel out, since the interstellar magnetic field direction varies strongly in different parts of the sky. Possible intrinsic (circumstellar or photospheric) effects are also likely to be randomly oriented within the sample.

In Tables 3-5 we list the values of the instrumental polarization, q_t and u_t, obtained for the UH88, T60, and H127 telescopes, respectively, for each run carried out. Statistical uncertainties are typically in the range $2-3\times10^{-6}$, and the values for each telescope do not change very much from one run to another. This is reassuring, since samples in different parts of the sky are used for different runs (seasons), and possible residual effects from interstellar polarization appear to be small. Obviously, there are slow long-term drifts and small jumps from mirror cleaning or other effects from the telescope optics.

We have excluded from the instrumental polarization computation stars with significant polarizations detected, and applied a simple iterative procedure in calculating the average q and u from the sample to provide q_t and u_t in each of the *BVR* passbands separately. These values, q_t and u_t, are then subtracted from the observed q and u in each passband for all of the observed stars. The telescopes we use for the present work (UH88, T60, and H127) are equatorially mounted, which is convenient in the sense that the telescope polarization does not rotate on the sky. It only gives a constant shift in (q, u).

The superachromatic half-wave plates we use have a very good efficiency throughout the whole wavelength range of the Dipol-2 passbands (400-800 nm). Nevertheless, we have observed high polarization standard stars to check for the polarization scale calibration, and for the zero-point of position angles.

In each run at least two different large polarization standards were observed, typically both in the beginning and in the end of the run. The stars HD 25443, HD 161056, HD 204827, BD+25 727, and BD+59 389, have been used for this purpose. We have found evidence of small calibration coefficients (1.02–1.04) needed in the V and R passbands. Though these differences can be partially due to systematic errors in the published values (Hsu & Breger 1982; Turnshek et al. 1990; Schmidt et al. 1992), we have applied the corrections to bring our data into the system commonly used by other investigators. In any case, for the very small polarization degrees found in the present study, these scale corrections are entirely negligible.

3.2. Broad-band (400-800 nm) polarization

Tables 6-8 list the broad-band polarizations computed by weighted averaging of the normalized Stokes parameters q and u

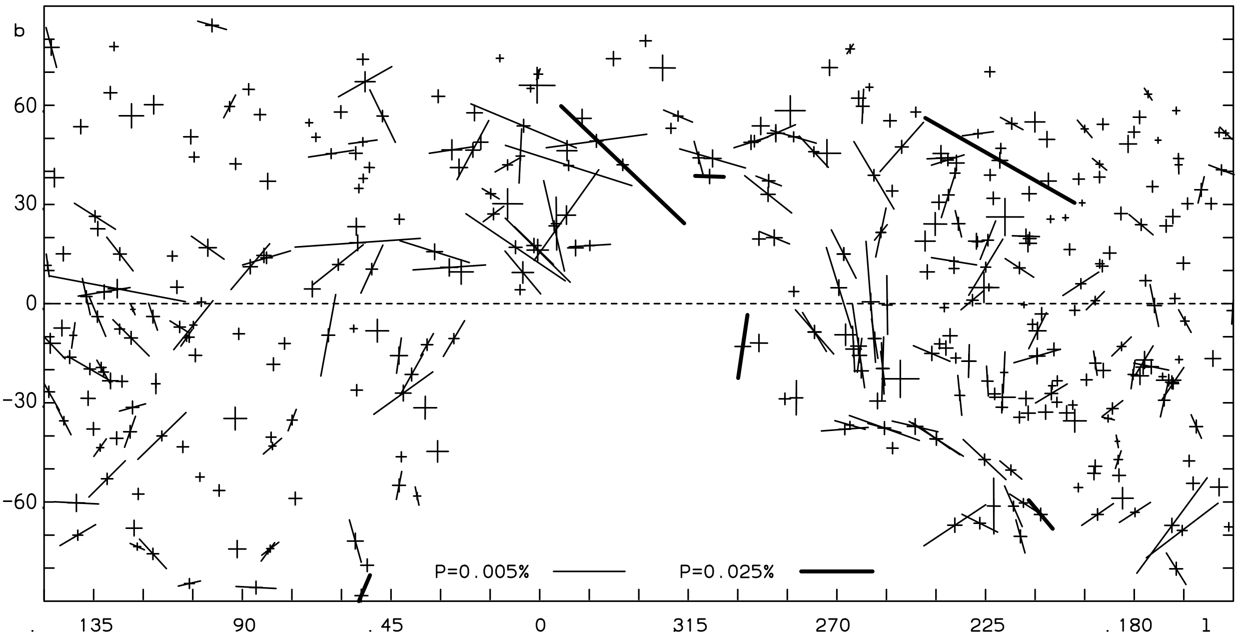

Fig. 3. Polarization map based on the observed sample of nearby stars ($d < 50$ pc), plotted in Galactic coordinates. The length of the bars is proportional to the degree of polarization and the orientation gives the direction of the maximum electric vector. Regions with aligned polarization vectors, suggesting filament-type structures, can be seen. Two different polarization scales are used for clarity, as indicated in the bottom of the panel. For low observed degrees of polarization, $p < 2\sigma$ (no detection), only a cross with bar lengths, σ, are plotted.

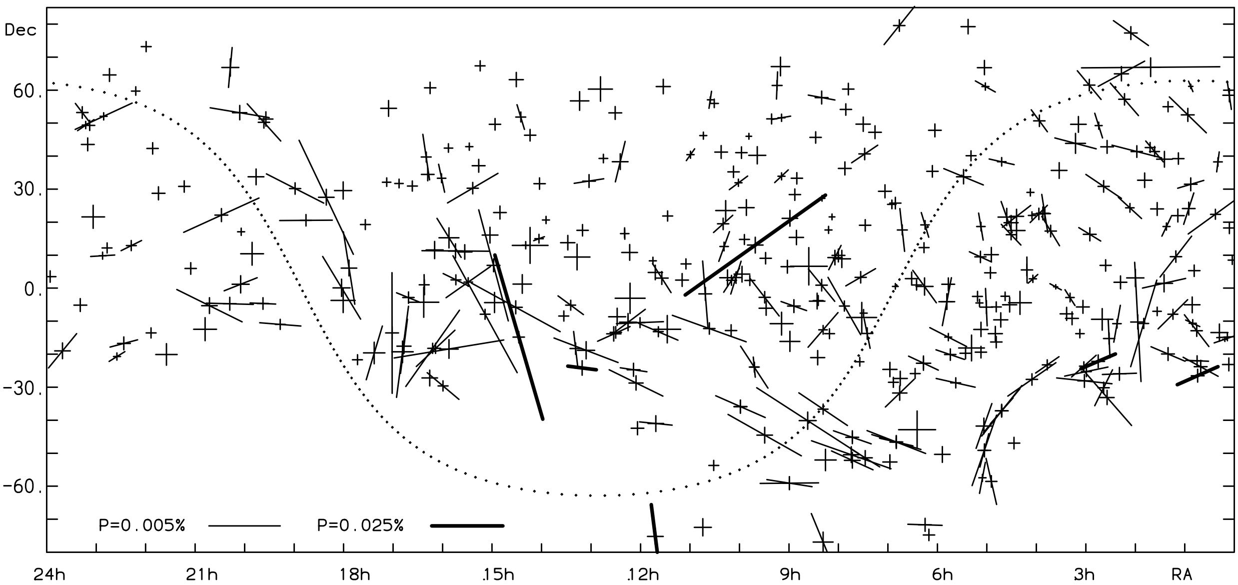

Fig. 4. Polarization map based on the sample of nearby stars ($d < 50$ pc), plotted in Equatorial coordinates. Two different polarization scales are used for clarity, as indicated in the bottom of the panel. For low observed degrees of polarization, $p < 2\sigma$ (no detection), only a cross with bar lengths, σ, are plotted. The dotted line shows the Galactic equator.

obtained in the B, V, and R, bands at the UH88, T60, and H127 telescopes, respectively. Statistically significant ($> 3\sigma$) polarizations are detected in 115 out of the 361 stars observed.

It is interesting to note the differences in the fraction of $> 3\sigma$ detections at the different telescopes. At the UH88 about 1/3 of the stars (43 of 125) show measurable polarization, whereas at the T60 the ratio is about 1/4 (49 of 205). This may be partially due to the fact that at UH88 somewhat fainter stars at larger distances were generally observed, and the effects from interstellar dust thereby are probably stronger. When identifying the target stars, the fainter magnitudes achievable with UH88 also made it possible to pick more reddened stars for a given distance compared to stars selected for T60. The data from H127 show the largest fraction of polarized stars, $\sim 2/3$ (23 of 31). This clearly indicates that the average dust content is larger in the direction of the H127 sample of stars (Southern hemisphere, $04^h < \alpha < 12^h, -77° < \delta < -4°$).

Figs. 3 and 4 show polarization maps based on the broadband data, plotted in the Galactic (l, b), and Equatorial coordinates. The general view may be a bit complicated, but there are several interesting features showing well aligned polarization vectors. Some of them look like 'arc' or 'loop'-like structures. One prominent example can be seen in the aforementioned region of the H127 sample of Southern stars ($200° < l <$

Table 3. Instrumental polarization of the UH88 telescope in the B, V, and R passbands, in units of 10^{-6} (ppm), for the observing runs in 2014-2016. The standard errors are in the range 2-4 ppm for each run.

JD Interval	q_{tB}	u_{tB}	q_{tV}	u_{tV}	q_{tR}	u_{tR}
2456818-6825	180	-231	57	-112	24	-74
2456849-6857	198	-258	43	-118	16	-72
2457284-7291	189	-247	48	-131	35	-86
2457413-7420	187	-252	64	-121	41	-82
2457431-7446	199	-227	57	-111	37	-76
2457556-7568	199	-243	53	-127	36	-84
2457645-7657	182	-251	55	-138	34	-91
2457671-7681	191	-238	56	-130	34	-99

Table 4. Instrumental polarization of the T60 telescope in the B, V, and R passbands, in units of 10^{-6} (ppm), for the observing runs in 2014-2018. The standard errors are in the range 2-3 ppm for each run.

JD Interval	q_{tB}	u_{tB}	q_{tV}	u_{tV}	q_{tR}	u_{tR}
2456994-6999	34	11	27	-3	44	-4
2457039-7047	-7	-7	2	-5	10	-6
2457154-7172	3	-14	6	-5	17	-11
2457205-7256	-32	-27	-30	-2	-29	2
2457297-7304	-7	-4	-25	3	-22	18
2457354-7370	1	-15	-25	-1	-39	12
2457490-7503	-2	-22	-24	-13	-31	-2
2457686-7701	-24	-26	-36	3	-47	13
2457774-7786	-11	-23	-30	1	-53	5
2457894-7895	-11	-30	-12	-9	-19	2
2458025-8113	-27	-20	-27	4	-29	9
2458134-8196	-12	-19	-24	5	-30	15
2458316-8352	-20	-26	-34	5	-50	-11
2458406-8452	-24	-13	-40	9	-49	28
2458455-8508	-16	-26	-35	-6	-47	1

Table 5. Instrumental polarization of the H127 telescope in the B, V, and R passbands, in units of 10^{-6} (ppm), for the observing runs in 2017 and 2018. The standard errors are in the range 2-4 ppm for the first run, and 4-8 ppm for the second run. The change in instrumental polarization from 2017 to 2018 is due to operations with the main mirror.

JD Interval	q_{tB}	u_{tB}	q_{tV}	u_{tV}	q_{tR}	u_{tR}
2457775-7799	-90	-3	-49	-9	-43	-1
2458125-8183	175	207	81	108	48	90

315°, −75° < b < 0°). Further observations would be useful to establish the polarization features in this interesting region in greater detail. We also note that the uncertainty of the instrumental polarization determination is somewhat larger for the H127 sample, particularly for the second run (Table 5), due to significant amount of polarization in most of the observed stars.

When comparing our map with earlier published data on nearby star polarization by Cotton et al. (2017), we can see similarities in the position angle patterns, particularly near the longitudes $l \sim 0°$ and $l = 260° - 315°$, even though the samples of observed stars are entirely different and also extend in their work to longer distances ($d > 50$ pc) than in our data.

The polarization position angle patterns (Figs. 3 and 4) suggest that the polarizing dust grains are aligned along magnetic filaments, some with spatial extents larger than 90°. Combined with data from several literature sources Frisch et al. (2015a) found that the position angles for stars in the longitude range $l = 315° - 60°$ reveal a filament in the direction toward the heliosphere nose region, as defined by the flow of interstellar neutral gas through the heliosphere ($l \sim 4°, b \sim 15°$). Our data (Fig. 3) also clearly show a filament in the opposite direction ($l \sim 180°, b \sim -15°$) corresponding to the (spatially broader) region of the heliosphere tail.

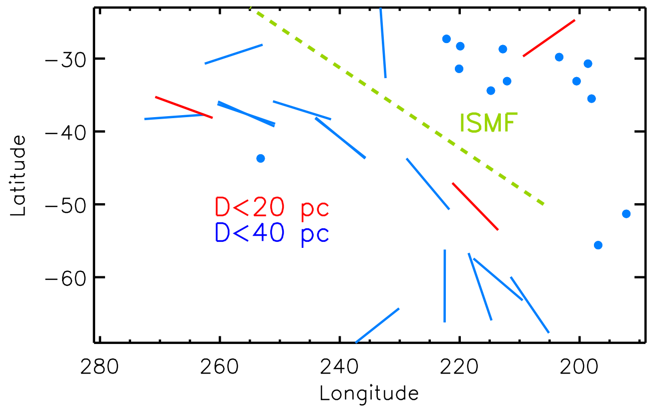

Fig. 5. Polarization position angles (bars) of a magnetic filament that is roughly parallel to the interstellar magnetic field shaping the heliosphere, are plotted for stars within 20 (red) and 40 (blue) parsecs. Stars with p/e_p less than 1.95 are plotted as dots. The green dashed line indicates the direction of the ISMF shaping the heliosphere as determined from the center of the IBEX ribbon of ENAs (see Sect. 3.2). Data are plotted in galactic coordinates (l, b).

High-sensitivity measurements of the polarizations of nearby stars provide the only methodology capable of connecting the ambient ISMF with the ISMF shaping the heliosphere (Frisch et al. 2015a). The interstellar magnetic field shaping the heliosphere was discovered to be traced by a "ribbon" of energetic neutral atoms (ENAs) formed by charge-exchange between interstellar neutral hydrogen atoms and plasma beyond the heliopause that separates solar and interstellar plasma (McComas et al. 2009). Modeling of the magnetic field creating the IBEX ribbon (Zirnstein et al. 2016) yields an interstellar magnetic field direction toward $l = 26°$, $b = 50°$. The newly discovered filament (Figs. 3 and 5) that is centered near $l = 240°$, $b = -42°$, roughly follows the direction of the IBEX ribbon ISMF. Several stars in this filament are within 20 pc, and the nearest star, HD 33262, is 12 pc away. These new polarization data firmly place the filament within the cluster of local interstellar clouds flowing past the Sun and extending to the solar location (Frisch et al. 2011). The new filament is also aligned with the projected interface between two of these local clouds, Dorados and the Blue Cloud, which have boundaries parallel to each other and the polarization filament, and have quasi-perpendicular velocities through the Local Standard of Rest (Frisch, Piirola, Berdyugin 2020, in preparation).

Efforts to evaluate the correspondence between polarization strengths and interstellar column densities for nearby stars have been unsuccessful because of the low column densities and unknown levels of ionization in the gas (Frisch et al. 2015b). Extended regions with stars lacking significant polarizations are also found, which can indicate very low dust content, nearby depolarization screens, or regions at the poles of the magnetic field.

Table 8. Broad-band (400-800 nm) polarimetric data of nearby stars observed at the H127 telescope. The normalized Stokes parameters, q and u, and the degree of polarization, p, are given in units of 10^{-6} (ppm), and the position angle θ in the Equatorial frame of references.

HD	R.A.	Decl.	$l(°)$	$b(°)$	V_{mag}	Par.	Sp	q	u	p	$\pm e_p$	$\theta(°)$	$\pm e_\theta(°)$
28454	04 27 06.0	-46 56 51	253.18	-43.71	6.10	30.54	F5.5V	0	1	1	± 8	56.7	± 41.2
29992	04 42 03.5	-37 08 40	239.92	-40.91	5.05	34.75	F3VI	8	-38	40	± 7	140.8	± 5.0
31746	04 54 53.0	-58 32 52	267.62	-37.96	6.11	32.82	F5V	29	14	33	± 8	13.1	± 7.1
32743	05 02 48.7	-49 09 05	255.64	-37.63	5.37	38.22	F5V	21	-12	24	± 5	164.9	± 5.3
32820	05 03 54.0	-41 44 42	246.33	-37.15	6.30	31.51	F8V	25	-21	33	± 11	160.4	± 9.7
33262	05 05 30.7	-57 28 22	266.03	-36.72	4.71	86.02	F9V	20	-8	22	± 5	169.6	± 5.9
38858	05 48 34.9	-04 05 41	209.38	-15.84	5.97	65.55	G2V	31	-12	34	± 11	169.2	± 9.0
40105	05 54 10.8	-50 21 45	257.71	-29.44	6.52	28.00	K1IV	21	5	22	± 11	7.0	± 13.6
43834	06 10 14.5	-74 45 11	285.76	-28.80	5.09	97.90	G7V	-8	-9	12	± 8	114.2	± 16.9
44447	06 15 06.0	-71 42 10	282.28	-28.49	6.62	30.71	G0V	-24	1	24	± 9	88.3	± 10.6
45289	06 24 24.4	-42 50 51	250.79	-22.76	6.67	35.87	G2V	-1	28	28	± 26	46.3	± 21.8
49095	06 45 22.9	-31 47 37	241.29	-15.08	5.92	41.65	F6.5V	-1	-28	28	± 10	133.6	± 9.9
50223	06 49 54.6	-46 36 52	256.12	-19.60	5.14	39.70	F5.5V	-25	16	30	± 8	73.9	± 7.4
52298	06 57 45.4	-52 38 54	262.63	-20.34	6.94	26.98	F8V	6	18	19	± 10	35.1	± 14.1
59468	07 27 25.5	-51 24 09	263.15	-15.64	6.71	44.48	G6.5V	-11	22	24	± 10	58.0	± 11.2
62644	07 42 57.1	-45 10 23	258.58	-10.58	5.04	44.50	G8IV-V	-20	14	24	± 6	72.8	± 7.4
62848	07 43 21.5	-52 09 51	264.96	-13.74	6.68	33.71	F9V	-21	24	32	± 11	65.9	± 9.3
63008	07 44 12.5	-50 27 24	263.45	-12.84	6.63	33.24	F9V	-46	37	59	± 11	70.8	± 5.1
69655	08 15 25.2	-52 03 37	267.35	-9.41	6.62	36.96	G1V	16	-16	23	± 15	158.0	± 17.0
70060	08 18 33.3	-36 39 33	254.78	-0.42	4.40	34.93	A8V	-16	37	41	± 7	56.5	± 4.8
71243	08 18 31.6	-76 55 11	289.86	-21.68	4.05	51.12	F5V	30	30	43	± 14	22.5	± 8.7
73524	08 37 20.0	-40 08 52	259.75	0.53	6.55	36.18	G0Vp	-35	77	85	± 12	57.3	± 4.2
77370	08 59 24.2	-59 05 01	276.79	-8.57	5.16	38.18	F4V	-36	5	36	± 6	86.4	± 5.0
82241	09 29 28.6	-44 31 57	269.43	4.81	6.97	24.07	F8V	-31	50	59	± 11	60.9	± 5.1
84117	09 42 14.4	-23 54 56	256.70	21.52	4.94	67.47	F9V	14	33	35	± 7	33.4	± 5.2
86629	09 58 52.3	-35 53 28	267.94	15.00	5.22	30.06	F1V	-18	15	24	± 10	69.6	± 11.9
91324	10 31 21.8	-53 42 56	283.04	3.66	4.89	45.61	F9V	2	13	13	± 7	41.5	± 14.5
93372	10 44 27.0	-72 26 37	293.60	-11.91	6.26	31.10	F6V	22	-6	22	± 12	172.2	± 14.5
101614	11 41 26.2	-41 01 06	288.96	19.95	6.87	28.80	G0V	-23	5	23	± 11	84.2	± 12.3
101805	11 42 14.9	-75 13 38	298.47	-12.96	6.47	29.35	F8V	216	57	223	± 11	8.7	± 1.4
104731	12 03 39.6	-42 26 03	293.60	19.57	5.15	40.44	F5V	-11	10	15	± 9	69.8	± 14.8

The star HD 83683 in the T60 data shows much stronger polarization than the others: $P(\%) = 0.0602 \pm 0.0011, \theta_{eq} = 125.2° \pm 0.5°$. This star is in the direction of a known nearby dust cloud ($l \sim 220°, b \sim 43°$) inside the local bubble (Meyer et al. 2006; Peek et al. 2011). Fitting the Serkowski law (Serkowski 1973) to the polarization data in the B, V, and R bands yields: $p_{max} = 0.0649 \pm 0.0008$ percent, $\lambda_{max} = 0.706 \pm 0.017 \mu$m. Polarization peaking in the red wavelengths indicates size distribution of scattering particles somewhat larger than average in the interstellar medium.

The star HD 101805 in the H127 data (Table 8) shows larger polarization than other stars in the sample ($p = 0.0223 \pm 0.0011$ percent), most likely due to a contribution of circumstellar origin (Sect. 3.3).

In the UH88 data the star HD 126679 ($l \sim 335°, b \sim 42°$) shows higher polarization, $P = 0.0595 \pm 0.0008$ percent, $\theta_{eq} = 16.4° \pm 0.4°$, but the wavelength dependence looks normal interstellar ($\lambda_{max} = 0.501 \pm 0.060 \mu$m, $p_{max} = 0.0623 \pm 0.0012$ percent).

Fig. 6 shows the dependence of observed polarization with distance. Since the degree of polarization is always positive, for small polarizations the observational errors bias the polarization towards higher values. Statistically, this can be corrected by $p_c = \sqrt{p^2 - \epsilon^2}$, where p is the observed degree of polarization and ϵ its error (see Serkowski 1962). For $p < \epsilon$, we adopt $p_c = 0$. The upper boundary of the points in Fig. 6 gives a dependence of maximum polarization with distance, $p\, d^{-1} \sim 2.9$ ppm pc^{-1}. Linear fit to all points gives $p\, d^{-1} = 0.37 \pm 0.14$ ppm pc^{-1}. This is much less than the value 1.64 ± 0.30 ppm pc^{-1} derived by Cotton et al. (2017) from a sample of Southern hemisphere stars. The majority of observed points in Fig. 6 lie well below the upper boundary, indicating very low contents of interstellar dust. There are large regions on the sky with no detectable polarization (see also Figs. 3 and 4), up to distances $d = 40 - 50$ pc. The viewing angle between the interstellar magnetic field and the line of sight also contributes to the low observed polarization.

3.3. Evidence of intrinsic effects from wavelength dependence, and/or variability of polarization

Three-colour (BVR) polarimetric data obtained for the star HD 101805 (Table 9) show polarization increasing from $p = 0.0172 \pm 0.0019$ percent in the R-band to $p = 0.0314 \pm 0.0018$ percent in the B-band. This suggests contribution from *small* scattering particles (Rayleigh-type scattering) in a circumstellar dust/gas envelope. Further studies of the circumstellar environment of HD 101805 would be desirable.

For the majority of the nearby stars ($d < 50$ pc) observed, the degree of polarization in the B, V, and R passbands is very

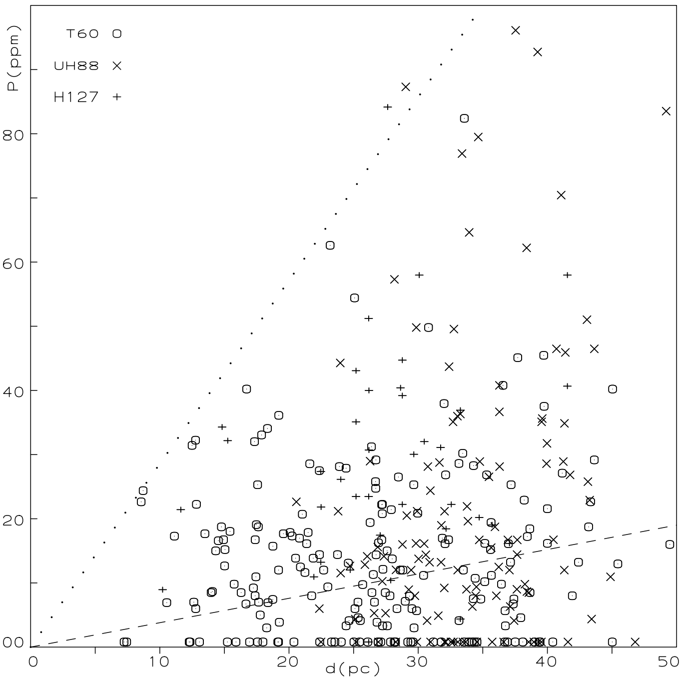

Fig. 6. The observed degree of polarization, p_c, corrected for the positive bias (see Sect. 3.2), plotted vs. distance, d. Upper boundary gives the relation, $p_c \sim 2.9$ ppm pc^{-1}, and linear fit to all points (dashed line), $p_c = 0.37 \pm 0.14$ ppm pc^{-1}.

Table 9. Evidence of intrinsic polarization in the star HD 101805 from a peculiar wavelength dependence. The polarization increases from the red towards the blue. The normalized Stokes parameters, q and u, and the degree of polarization, p, are given in units of 10^{-6} (ppm), and the position angle θ in the Equatorial frame of references.

Filter	q	u	$p \pm e_p$	$\theta \pm e_\theta(^\circ)$	J.D.
B	306	72	314 ± 18	6.6 ± 1.7	7799.1965
V	175	70	188 ± 19	10.8 ± 2.9	7799.1965
R	164	52	172 ± 19	8.8 ± 3.2	7799.1965

low, and constraining the properties of interstellar or circumstellar dust by the wavelength dependence is difficult.

We have observed several stars on more than one night. Multiple observations give the possibility to look for variability on long time intervals, from weeks to years. As an initial approach we have adopted a criterium for picking up candidates for variable polarization: to choose stars which show the standard deviation of the normalized Stokes parameters q and $u >$ *twice* what is expected from the errors of the nightly points. Table 11 lists measurements of stars which give evidence of variable polarization from the data obtained at the T60 telescope. The majority of our multiple observations were made with T60.

From the total of 205 stars observed at T60 there are 18 stars showing standard deviation of q and u larger than twice what is expected from the errors of the nightly points (Table 11). A few stars show ($> 3\sigma$) night-to-night changes. The clearest examples are HD 19373, HD 58855, and HD 205289, where statistically signifigant deviations of either q or u parameter from their mean values are found, at the 2-3$\times10^{-5}$ level. Still, the evidence for variability is rather marginal, and polarization variations exceeding 10^{-5} do not appear to be common in inactive F-G main

Table 10. Stars with multiple observations from the H127 telescope. The normalized Stokes parameters, q and u, and the degree of polarization, p, are given in units of 10^{-6} (ppm), and the position angle θ in the Equatorial frame of references.

HD	q	u	$p \pm e_p$	$\theta \pm e_\theta(^\circ)$	J.D.
29992	7	-38	40 ± 8	140.0 ± 5.4	7777.9542
29992	10	-43	45 ± 5	141.3 ± 3.1	7787.9810
29992	3	-22	24 ± 9	138.3 ± 10.5	8134.9991
	8	-38	40 ± 7	140.8 ± 5.0	av.
32743	21	-11	24 ± 5	164.9 ± 5.3	7778.0907
32743	41	-32	52 ± 9	160.7 ± 4.8	7781.9548
	26	-16	31 ± 16	163.3 ± 13.5	av.
50223	-29	20	36 ± 8	73.2 ± 6.0	7775.0941
50223	-20	10	24 ± 5	77.3 ± 6.3	7782.8461
50223	-32	30	44 ± 9	68.9 ± 5.9	8125.9939
	-24	16	30 ± 8	73.9 ± 7.4	av.
62644	-14	6	16 ± 9	79.5 ± 14.6	7778.0816
62644	-21	17	28 ± 6	71.0 ± 6.5	7799.0168
	-19	14	24 ± 6	72.8 ± 7.4	av.
77370	-40	0	41 ± 9	90.6 ± 6.5	7781.1073
77370	-29	10	32 ± 9	81.2 ± 7.6	7782.1288
	-35	5	36 ± 6	86.4 ± 5.0	av.
86629	-25	28	38 ± 9	66.5 ± 6.3	7778.1918
86629	-9	3	10 ± 9	81.2 ± 20.5	7782.1653
	-17	15	24 ± 10	69.6 ± 11.9	av.

sequence stars. More observations are needed to find evidence for possible periodicity or other systematic time variability.

In our data from the H127 telescope there are 5 stars observed more than once (Table 10). None of these stars shows statistically significant deviations of q and u from their mean values, i.e., variations are $< 2\sigma$.

We have additional polarization data from observations made at the WHT telescope, and at the Nordic Optical Telescope (NOT), at ORM, La Palma. The copy of Dipol-2 polarimeter used at the WHT is the one currently at H127. At the NOT a new version (Dipol-UF) is used. This instrument is equipped with high speed readout EMCCD cameras, otherwise the instrument principle is similar to that of Dipol-2.

The star HD 6715 shows somewhat stronger polarization, $p(\%) = 0.0036 \pm 0.0009$, in our measurements at the WHT (Table 12) than observed at the UH88 (Table 6), $p(\%)=0.0007 \pm 0.0009$, indicating possible intrinsic effects. The polarized star HD 132307 observations at WHT and UH88 are in agreement, within the errors.

The stars observed at the NOT (Table 13) were already measured at the T60 telescope (Table 7). The results are in good agreement. The star HD 191195 gives a $> 3\sigma$ detection at both telescopes: $p(\%) = 0.0042 \pm 0.0010, \theta = 80.7^\circ \pm 7.0^\circ$, and $p(\%) = 0.0039 \pm 0.0008, \theta = 68.2^\circ \pm 5.6^\circ$, at the T60 and the NOT, respectively.

3.4. Comparison of polarization maps at high Northern galactic latitudes for the nearby and distant stars

Fig. 7 gives a polarization map for the nearby stars at Northern galactic latitudes, for comparison with earlier results for more distant stars (Berdyugin et al. 2014). The most prominent feature seen in the Northern ($b > 30^\circ$) high latitude polarization map for the distant ($d \geq 100$ pc) stars is a giant "arc" or "loop" between

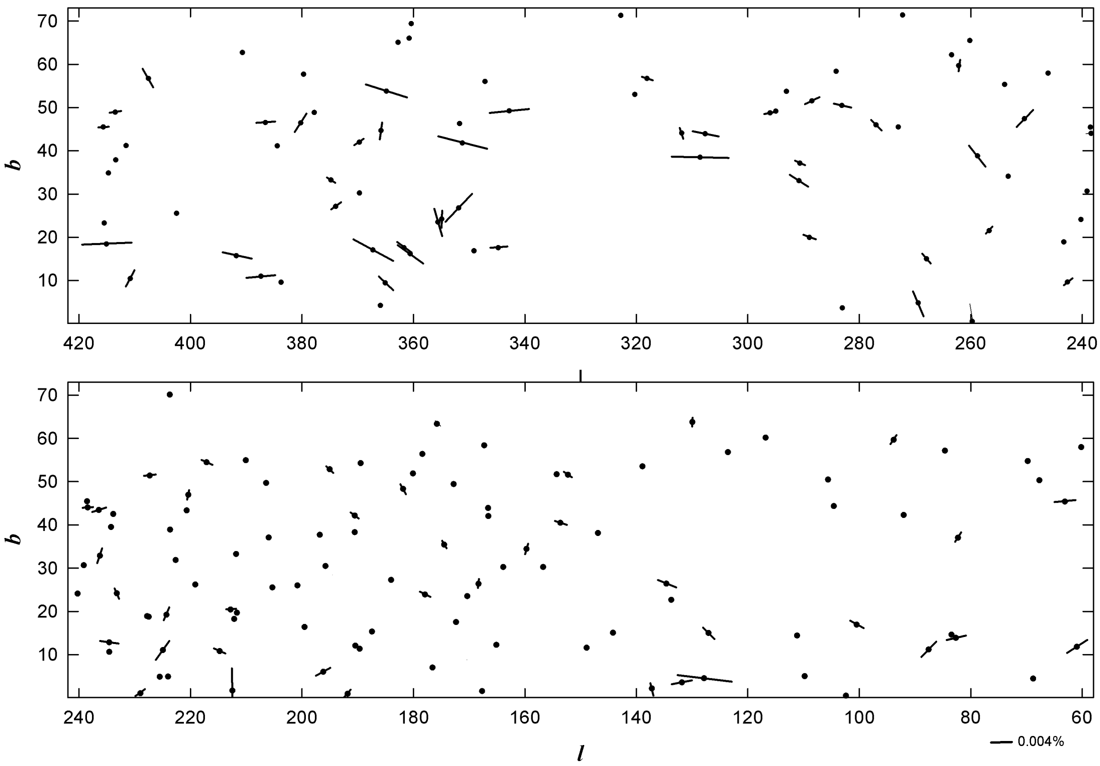

Fig. 7. Polarization map of Northern Galactic latitude ($b > 0°$) nearby stars ($d < 50$pc), shown for comparison with earlier published results of more distant stars (Fig. 8). The polarizations for the peculiar stars HD 83683 and HD 126679 are not shown here.

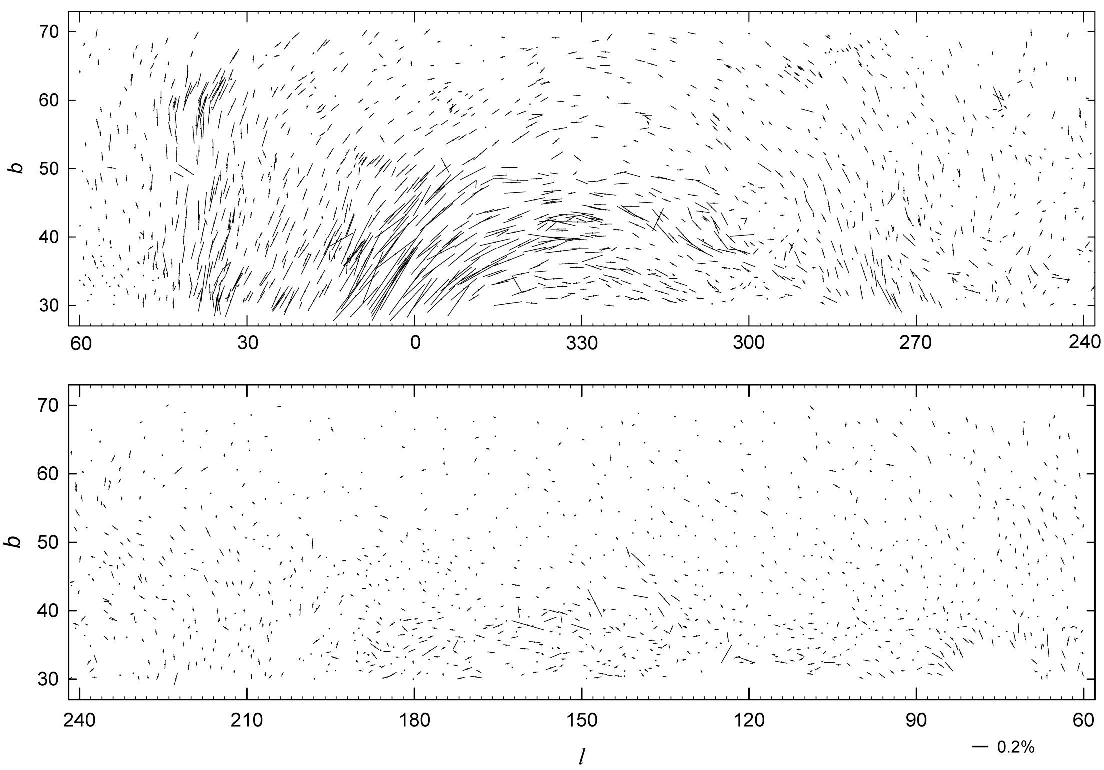

Fig. 8. Polarization map of Northern Galactic latitude stars in the distance range 100 pc $< d <$ 500 pc. Note that the polarization scale is compressed by a factor of ∼70 compared with that in Fig, 7, and only stars with $b > 30°$ are plotted (from Berdyugin et al. 2014).

Table 12. Broad-band (400-800 nm) polarimetric data of nearby stars observed at the WHT telescope. The normalized Stokes parameters, q and u, and the degree of polarization, p, are given in units of 10^{-6} (ppm), and the position angle θ in the Equatorial frame of references.

HD	q	u	$p \pm e_p$	$\theta \pm e_\theta(^\circ)$	J.D.
6715	7	35	36 ± 9	39.7 ± 6.8	7407.3626
18144	8	-1	8 ±11	178.1 ±27.4	7407.4020
42182	-8	27	28 ±12	53.4 ±11.2	7407.4430
51219	-19	-32	38 ±11	119.6 ± 8.1	7407.4797
65629	7	-13	14 ±10	149.4 ±17.1	7407.5174
77278	-7	11	13 ± 9	60.4 ±17.2	7407.5700
117860	4	16	16 ± 5	37.9 ± 8.2	7206.3865
132307	58	18	61 ± 8	8.5 ± 3.8	7207.3826
140667	-27	8	28 ± 8	81.3 ± 8.1	7208.3825
145229	-18	5	19 ±14	82.2 ±18.6	7209.3942
150433	-21	9	23 ± 6	79.1 ± 6.8	7206.4277
225261	-21	-38	43 ± 9	120.6 ± 5.6	7407.3097

Table 13. Broad-band (400-800 nm) polarimetric data of nearby stars observed at the NOT telescope. The normalized Stokes parameters, q and u, and the degree of polarization, p, are given in units of 10^{-6} (ppm), and the position angle θ in the Equatorial frame of references.

HD	q	u	$p \pm e_p$	$\theta \pm e_\theta(^\circ)$	J.D.
4813	2	-6	6 ± 7	142.2 ± 25.2	8687.6996
132052	-3	10	11 ± 9	53.0 ± 19.2	8687.3744
132254	10	-8	13 ± 8	160.3 ± 15.5	8688.3977
142373	12	19	22 ± 9	28.7 ± 11.0	8688.3748
147449	6	3	7 ± 9	15.2 ± 26.2	8688.4173
187013	-21	-17	27 ± 7	109.3 ± 7.6	8688.5784
187691	-15	-12	19 ± 6	109.6 ± 8.6	8687.5400
191195	-28	27	39 ± 8	68.2 ± 5.6	8687.5638
205289	-3	4	5 ± 8	65.8 ± 29.1	8687.5828
207958	-8	-9	12 ± 8	114.0 ± 16.4	8687.6414
213558	3	-4	5 ± 6	156.5 ± 25.4	8688.7006
215648	-16	-22	27 ± 7	116.7 ± 7.0	8687.6184
218470	1	-6	6 ± 7	140.6 ± 23.0	8687.6590
219623	13	-9	15 ± 7	162.4 ± 12.3	8688.7211
225003	-5	-21	21 ± 6	128.1 ± 8.1	8687.6780

the longitudes 270° – 45°, with the center at l = 330° (Fig. 8). There is a striking difference between the longitude range l = 240° – (360°) – 60° (top panel of Fig. 8), where polarizations are strong and well aligned, and the range l = 60° – 240° (bottom panel of Fig. 8), where polarizations are much smaller and no clear alignment patterns are visible.

The number of observed nearby stars in Fig. 7 is small, but comparison with Fig. 8 shows similar features: larger polarizations in l = 240° – (360°) – 0°, and smaller values in l = 60° – 240°. There is also evidence for the "arc" structure seen on the top panel. Accordingly, local magnetic field structures seen in the distance range 100 pc – 500 pc also appear at closer distances. This result is consistent with a position of the Sun inside the Local Bubble where more nearby interstellar dust is found in the galactic center hemisphere than in the anti-center hemisphere (Frisch & Dwarkadas 2017).

4. Conclusions

We have collected an extensive high S/N polarization dataset of 361 nearby stars (d < 50 pc). Polarization maps based on these data show patterns of aligned polarization vectors, correlating with known nearby dust clouds.

The polarization position angles show that the very local ISMF is arranged into distinct magnetic filaments, some with spatial extents larger than 90°. These magnetic filaments provide a new perspective on the structure of local interstellar clouds that are historically identified primarily by cloud kinematics. There are large regions on the sky with no detectable polarizations ($p < 10^{-5}$), up to distances $d = 40 - 50$ pc, which indicates very low dust content in these areas, particularly on the Northern sky. Linear fit to our sample gives a relation for the average dependence of the degree of polarization vs. distance, $p\ d^{-1} = 0.37 \pm 0.14$ ppm pc^{-1}. This is smaller by a factor of about 4 than values found for representative regions in the Southern hemisphere (Cotton et al. 2017). However, the scatter is large and the values for individual stars in our dataset are in the range $0 < p\ d^{-1} < 2.9$ ppm pc^{-1}. Beyond this, there are a few outliers. The extreme case is HD 83683 which is located in a known nearby dust cloud and has $p\ d^{-1} = 14.8 \pm 0.2$ ppm pc^{-1}.

From long-term multiple observations a number (∼ 20) of stars give marginal evidence of intrinsic variability at the 10^{-5} level. Three stars show statistically significant (> 3σ) night-to-night changes. These can be addressed to circumstellar effects (e.g. debris disks, chromospheric activity). The star HD 101805 shows a peculiar wavelength dependence with a steep gradient, indicating size distribution of scattering particles different from that of a typical interstellar medium.

Comparison of polarization maps at the high Northern galactic latitudes for the distant (100 pc < d < 500 pc), and for the nearby stars (d < 50 pc), shows similar features of polarization patterns, i.e., local magnetic field structures seen in the distance range d = 100 pc – 500 pc also extend to and appear at closer distances.

Our high S/N measurements of intrinsically inactive F-G stars in the magnitude range 3.8 < V < 9.1, with very low polarization, also provide a useful dataset for calibration purposes.

Acknowledgements. This work was supported by the ERC Advanced Grant HotMol ERC-2011-AdG-291659 (www.hotmol.eu). Dipol-2 was built in the cooperation between the University of Turku, Finland, and the Kiepenheuer Institut für Sonnenphysik, Germany, with the support by the Leibniz Association grant SAW-2011-KIS-7. We are grateful to the Institute for Astronomy, University of Hawaii for the observing time allocated for us on the UH88 and T60 telescopes, and to the University of Tasmania (UTAS) for the observing time at the H127 telescope. The Nordic Optical Telescope (NOT), and the William Herschel Telescope (WHT) are operated in the Spanish Observatorio del Roque de los Muchachos (ORM) of the Instituto de Astrophysica de Canarias (IAC). Greenhill Observatory is supported by the University of Tasmania Foundation. The H127 telescope is funded in part by grant LE110100055 from the Australian Research Council. The work of P. Frisch was funded by the IBEX mission as part of NASA's Explorer Program (80NSSC18K0237) and the IMAP mission as a part of NASA's Solar Terrestrial Probes Program (80GSFC19C0027).

References

Bailey, J., Kedziora-Chudczer, L., Cotton, D. V., et al. 2015, MNRAS, 449, 3064
Bailey, J., Lucas, P. W., & Hough, J. H. 2010, MNRAS, 405, 2570
Berdyugin, A., Piirola, V., Sadegi, S., et al. 2016, A&A, 591, A92
Berdyugin, A., Piirola, V., Sakanoi, T., Kagitani, M., & Yoneda, M. 2018, A&A, 611, A69
Berdyugin, A., Piirola, V., & Teerikorpi, P. 2014, A&A, 561, A24
Cotton, D. V., Marshall, J. P., Bailey, J., et al. 2017, MNRAS, 467, 873
Cotton, D. V., Marshall, J. P., Frisch, P. C., et al. 2019, MNRAS, 483, 3636
Frisch, P. & Dwarkadas, V. V. 2017, Effect of Supernovae on the Local Interstellar Material, 2253

Frisch, P. C., Andersson, B. G., Berdyugin, A., et al. 2015a, ApJ, 805, 60
Frisch, P. C., Berdyugin, A., Piirola, V., et al. 2015b, ApJ, 814, 112
Frisch, P. C., Redfield, S., & Slavin, J. D. 2011, ARA&A, 49, 237
Hsu, J. C. & Breger, M. 1982, ApJ, 262, 732
McComas, D. J., Allegrini, F., & Bochsler, P. e. a. 2009, Science, 326, 959
Meyer, D. M., Lauroesch, J. T., Heiles, C., Peek, J. E. G., & Engelhorn, K. 2006, ApJ, 650, L67
Peek, J. E. G., Heiles, C., Peek, K. M. G., Meyer, D. M., & Lauroesch, J. T. 2011, ApJ, 735, 129
Piirola, V. 1973, A&A, 27, 383
Piirola, V., Berdyugin, A., & Berdyugina, S. 2014, in Proc. SPIE, Vol. 9147, Ground-based and Airborne Instrumentation for Astronomy V, 91478I
Schmidt, G. D., Elston, R., & Lupie, O. L. 1992, AJ, 104, 1563
Schwadron, N. A., Bzowski, M., & Crew, G. B. 2009, Science, 326, 966
Serkowski, K. 1962, Advances in Astronomy and Astrophysics, 1, 289
Serkowski, K. 1973, in IAU Symposium, Vol. 52, Interstellar Dust and Related Topics, ed. J. M. Greenberg & H. C. van de Hulst, 145
Turnshek, D. A., Bohlin, R. C., Williamson, R. L., I., et al. 1990, AJ, 99, 1243
Zirnstein, E. J., Heerikhuisen, J., Funsten, H. O., et al. 2016, ApJ, 818, L18

Table 6. Broad-band (400-800 nm) polarimetric data of nearby stars observed at the UH88 telescope. The normalized Stokes parameters, q and u, and the degree of polarization, p, are given in units of 10^{-6} (ppm), and the position angle θ in the Equatorial frame of references.

HD	R.A.	Decl.	$l(°)$	$b(°)$	V_{mag}	Par.	Sp	q	u	p	$\pm e_p$	$\theta(°)$	$\pm e_\theta(°)$
101	00 05 54.7	18 14 06	108.00	-43.31	7.46	26.72	F8V	-6	-7	9	± 8	114.7	± 20.6
361	00 08 16.4	-14 49 28	81.53	-74.12	7.03	36.57	G1V	-15	-1	15	± 5	92.7	± 2.4
1562	00 20 00.4	38 13 39	116.17	-24.23	6.99	40.46	G1V	14	-4	14	± 6	172.5	± 7.2
1832	00 23 00.2	22 22 30	114.34	-40.02	7.59	24.57	F8V	-15	-45	47	± 7	125.7	± 4.4
4208	00 44 26.7	-26 30 57	53.97	-88.32	7.79	29.22	G7V	-105	-115	156	± 9	113.8	± 1.7
4915	00 51 10.8	-05 02 21	122.76	-67.91	6.97	44.48	G5V	1	10	10	± 11	42.8	± 23.1
5035	00 52 40.2	31 27 34	123.24	-31.41	8.36	24.71	G0V	-16	-10	19	± 9	106.5	± 12.4
5294	00 54 59.3	24 06 01	123.97	-38.76	7.38	33.43	G5V	19	-14	23	± 9	161.8	± 10.2
5372	00 56 17.4	52 29 29	123.68	-10.37	7.52	24.20	G5V	-2	36	36	± 9	46.2	± 6.8
6664	01 07 58.8	39 15 09	126.42	-23.51	7.78	27.99	G1V	7	-2	7	± 8	171.1	± 24.1
6715	01 08 12.5	21 58 37	128.06	-40.73	7.65	30.73	G5V	2	-6	7	± 9	142.4	± 26.8
7047	01 10 54.3	09 33 50	130.92	-53.01	7.21	25.28	G0V	9	-35	36	± 8	142.0	± 6.3
8004	01 20 36.9	54 57 45	127.15	-7.67	7.20	29.70	G0V	0	1	1	± 7	63.2	± 39.4
8129	01 20 30.0	-19 56 56	167.30	-80.21	7.59	32.32	G7V	-18	19	26	± 9	67.0	± 9.2
8262	01 22 17.9	18 40 58	133.04	-43.58	6.97	38.38	G2V	9	-12	15	± 5	154.3	± 9.2
8467	01 24 28.0	39 03 43	129.91	-23.36	8.20	30.24	G5V	0	3	4	± 11	55.3	± 35.9
8648	01 25 20.1	01 27 39	140.21	-60.27	7.39	25.04	G3V	-28	-13	31	± 12	102.5	± 10.4
9472	01 33 19.0	23 58 32	135.08	-37.91	7.63	30.25	G0V	11	9	15	± 9	19.7	± 15.5
10145	01 41 37.7	66 54 36	127.83	4.52	7.70	26.64	G6V	-97	-1	97	± 13	90.4	± 3.9
11926	01 58 04.6	41 23 10	136.14	-19.77	7.57	30.58	G5V	-31	17	36	± 8	75.8	± 7.6
12846	02 06 30.2	24 20 02	144.02	-35.44	6.88	42.01	G2V	-2	22	22	± 6	47.8	± 7.6
13403	02 12 56.1	57 12 16	133.83	-3.93	7.00	24.25	G3V	4	29	30	± 8	41.0	± 7.2
13783	02 16 49.2	64 57 09	131.81	3.56	8.31	25.25	G8V	-21	-31	37	± 10	118.3	± 7.4
15830	02 34 10.7	42 47 07	142.28	-16.19	7.60	31.21	G0V	6	4	7	± 9	17.4	± 26.1
16095	02 34 11.7	-33 07 03	234.30	-67.05	7.57	23.22	F7V	7	51	52	± 10	41.3	± 5.3
16397	02 38 27.9	30 49 00	148.57	-26.67	7.37	28.76	G0V	-12	28	30	± 8	56.2	± 7.2
17207	02 45 01.1	-22 10 00	208.30	-63.78	7.14	25.73	F7V	-91	-94	131	± 9	113.0	± 1.9
18144	02 55 17.4	16 18 33	161.23	-37.19	7.40	37.22	G8V	-8	16	18	± 9	58.7	± 12.7
19034	03 03 39.0	-05 39 59	184.61	-51.94	8.09	26.57	G5V	-9	-2	9	± 9	95.6	± 22.9
19467	03 07 18.6	-13 45 42	196.93	-55.63	7.00	31.23	G3V	9	6	11	± 6	16.8	± 14.0
19769	03 12 30.4	43 51 38	148.12	-12.00	7.56	28.19	G0V	-26	14	30	± 14	75.5	± 12.8
20619	03 19 01.9	-02 50 36	184.84	-47.18	7.04	41.67	G1V	6	12	13	± 6	32.4	± 13.1
21847	03 32 39.9	35 39 33	156.19	-16.60	7.30	19.22	F8V	16	13	21	± 11	19.7	± 13.7
23052	03 42 36.9	17 17 37	170.93	-29.21	7.08	48.62	G4V	11	21	24	± 8	31.2	± 9.6
23965	03 50 03.5	22 35 30	168.27	-24.16	7.29	23.18	F7V	26	8	27	± 8	8.8	± 8.3
24206	03 52 05.6	22 40 18	168.58	-23.78	7.57	33.45	G7V	6	-5	8	± 9	160.3	± 24.1
27466	04 19 57.1	-04 26 20	197.98	-35.45	7.82	26.98	G5V	16	-12	20	± 16	161.4	± 19.2
27808	04 24 14.6	21 44 11	174.83	-19.05	7.12	23.11	F8V	-7	-24	25	± 10	127.4	± 10.9
28483	04 30 18.0	19 50 26	177.33	-19.20	7.09	19.54	F6V	7	-6	9	± 10	157.7	± 24.3
28821	04 32 21.5	-05 02 20	200.47	-33.07	7.61	27.60	G3V	7	15	16	± 10	31.6	± 16.1
29150	04 36 14.0	21 32 12	176.88	-17.05	7.56	29.54	G5V	18	15	23	± 12	19.6	± 13.5
29980	04 43 16.4	-09 37 05	206.80	-32.80	8.06	19.80	G4V	2	12	12	± 10	41.2	± 19.6
31412	04 55 55.9	04 40 14	194.44	-23.03	7.02	27.74	F9V	-7	5	8	± 8	71.3	± 21.7
46090	06 31 21.5	02 54 41	208.05	-3.13	7.13	32.38	G4V	-5	-15	16	± 9	125.3	± 15.5
49736	06 51 00.4	25 45 37	189.65	11.34	6.94	29.03	F8V	-6	-5	8	± 8	107.8	± 22.2
58595	07 28 10.6	40 39 24	177.92	23.88	7.39	34.34	G5V	-8	-20	22	± 8	123.8	± 10.4
58781	07 27 50.8	19 02 41	199.54	16.37	7.24	34.17	G5V	0	-12	12	± 8	135.9	± 17.2
62522	07 47 57.2	60 17 46	156.73	30.24	7.02	25.67	F5V	0	-4	4	± 8	128.7	± 30.3
63814	07 52 15.6	36 16 12	184.00	27.25	7.07	23.03	F8V	7	-7	10	± 9	158.4	± 20.8
65629	07 59 53.4	09 53 55	211.67	19.66	7.98	29.25	G5V	-10	-1	11	± 9	93.8	± 20.5
66573	08 04 29.8	09 16 05	212.79	20.41	7.26	33.53	G5V	11	-15	19	± 10	152.9	± 13.3
72946	08 35 51.3	06 37 22	219.12	26.20	7.25	38.65	G8V	28	8	29	± 26	8.1	± 21.0
76780	08 58 55.7	21 09 59	205.96	37.08	7.63	26.55	G5V	-20	-3	20	± 11	94.9	± 14.6
77278	09 01 47.6	06 29 52	222.65	31.86	8.10	31.47	G5V	-10	-13	16	± 9	116.1	± 14.2
78612	09 08 49.8	-10 45 27	240.24	24.09	7.15	24.21	G3V	-10	-17	20	± 16	119.6	± 19.5
84749	09 47 22.9	02 18 55	234.24	39.49	7.70	21.37	F8V	0	-4	4	± 7	134.2	± 28.5
85689	09 53 48.4	14 44 20	220.39	46.96	7.69	22.28	G0V	-6	12	13	± 7	58.4	± 13.8
88072	10 09 23.4	02 22 16	238.43	44.02	7.55	27.82	G3V	8	-19	20	± 7	146.4	± 9.8

Table 6. continued.

HD	R.A.	Dec	$l(°)$	$b(°)$	V_{mag}	Par.	Sp	q	u	p	$\pm e_p$	$\theta(°)$	$\pm e_\theta(°)$
88725	10 14 08.3	03 09 05	238.54	45.44	7.73	28.80	G4V	6	-19	20	± 11	143.9	± 14.3
89307	10 18 21.3	12 37 16	227.30	51.40	7.04	31.21	G0V	17	-14	22	± 6	159.8	± 8.0
96937	11 09 40.2	02 27 23	253.94	55.33	9.11	33.95	G8V	-3	14	15	± 9	51.7	± 14.6
99505	11 27 03.2	21 51 08	223.71	70.12	7.62	30.56	G5V	1	-6	6	± 7	141.6	± 16.4
99610	11 27 30.2	-12 26 09	273.00	45.50	7.39	28.95	G4V	-12	11	16	± 19	69.1	± 25.2
101690	11 42 07.3	04 44 50	263.44	62.18	7.34	26.14	G0V	13	-5	14	± 10	169.2	± 17.8
104982	12 05 13.4	-28 43 02	290.83	33.07	7.82	27.56	G2V	-26	33	42	± 10	64.1	± 6.4
106116	12 12 28.8	-03 05 04	284.15	58.36	7.50	28.98	G5V	10	-21	23	± 21	147.8	± 20.9
106210	12 13 13.1	10 49 18	272.23	71.38	7.56	27.07	G3V	-16	11	20	± 11	72.7	± 14.5
106516	12 15 10.6	-10 18 45	288.50	51.54	6.11	44.74	F9V	0	-10	10	± 8	134.5	± 19.2
107146	12 19 06.5	16 32 54	266.00	77.04	7.03	36.40	G2V	8	0	8	± 6	1.1	± 6.7
108076	12 24 45.9	38 19 08	147.81	77.49	8.03	23.95	G0V	26	-13	29	± 11	166.3	± 10.7
108510	12 27 55.5	-08 40 41	293.07	53.74	6.74	34.74	G1V	13	15	20	± 12	23.9	± 15.6
113319	13 02 33.5	32 26 00	99.15	84.17	7.55	31.45	G4V	-20	-6	21	± 9	98.7	± 11.4
113720	13 05 46.2	-18 49 33	307.64	43.91	8.35	22.92	G5V	-36	32	48	± 12	69.2	± 7.0
114432	13 10 46.6	-24 10 45	308.57	38.48	7.84	29.55	G7V	-97	25	101	± 10	82.7	± 2.9
115043	13 13 37.0	56 42 30	116.81	60.16	6.81	39.70	G1V	-2	-6	6	± 13	127.7	± 32.5
117860	13 33 11.3	-08 26 36	320.26	53.02	7.36	29.89	G2V	-3	-2	4	± 7	102.4	± 31.3
121320	13 54 28.2	20 38 30	12.05	74.22	7.89	31.69	G5V	-2	7	7	± 5	54.9	± 18.0
122652	14 02 31.6	31 39 39	53.51	73.89	7.15	25.29	F8V	-5	0	5	± 8	92.5	± 28.8
122676	14 02 56.9	14 58 31	0.39	69.40	7.14	37.61	G7V	-6	-5	8	± 6	110.2	± 7.4
124694	14 13 51.3	46 19 31	88.08	64.83	7.16	25.44	F8V	5	-3	6	± 8	163.7	± 26.8
126679	14 27 21.4	-14 50 20	334.85	42.01	7.32	21.94	F7V	500	322	595	± 8	16.4	± 0.4
127352	14 31 00.6	-05 48 08	342.80	49.21	7.69	24.35	K0V	-39	60	71	± 9	61.5	± 3.4
131042	14 50 41.0	22 54 27	30.68	62.72	7.51	26.94	G2V	-5	-10	11	± 9	122.2	± 19.5
132307	14 58 10.9	06 54 18	4.85	53.77	8.18	28.86	G5V	69	41	80	± 9	15.1	± 3.1
133161	15 02 33.1	16 03 18	19.70	57.69	7.02	26.03	G2V	-11	9	14	± 11	71.3	± 19.4
134088	15 08 12.6	-07 54 48	351.22	41.78	9.02	25.48	G2V	49	79	93	± 7	29.0	± 2.2
135891	15 16 21.4	37 04 10	60.19	57.96	7.10	25.94	F8V	3	-1	3	± 9	168.2	± 34.9
138004	15 27 40.4	42 52 53	69.79	54.75	7.48	31.13	G2III	0	4	4	± 5	47.8	± 18.0
138573	15 32 43.7	10 58 06	17.79	48.84	7.19	33.30	G5IV-V	-14	10	17	± 10	72.4	± 15.2
140667	15 44 31.8	11 15 59	20.21	46.44	7.53	24.16	G0V	-47	1	47	± 10	89.5	± 6.3
141937	15 52 17.5	-18 26 10	351.89	26.78	7.25	29.95	G1V	-74	-25	78	± 13	99.2	± 4.7
142093	15 52 00.6	15 14 09	26.56	46.51	7.33	31.60	G2V	14	28	32	± 14	31.9	± 12.2
143114	15 59 38.3	-29 37 57	344.79	17.56	7.33	27.55	G0V	-5	29	29	± 7	50.1	± 6.8
144766	16 08 07.1	-18 14 35	354.92	24.20	7.03	30.06	F9V	-3	-37	37	± 7	132.9	± 5.3
145229	16 09 26.6	11 34 28	24.42	41.13	7.44	29.64	G0V	-14	5	15	± 12	79.3	± 19.4
145518	16 12 02.5	-18 13 57	355.61	23.51	7.41	29.46	G0.5V	21	-62	65	± 7	144.6	± 3.2
146070	16 15 19.1	-27 12 37	349.14	16.85	7.54	28.05	G1V	9	-17	19	± 11	149.4	± 14.6
146868	16 14 57.1	60 40 11	92.03	42.27	7.68	32.30	G4V	0	1	1	± 8	50.5	± 43.0
147044	16 18 05.9	34 28 58	55.65	45.49	7.49	26.56	G0V	16	6	17	± 9	9.8	± 13.9
147512	16 22 32.7	-04 14 57	9.69	30.21	7.33	37.15	G8/K0V	-16	5	17	± 21	81.1	± 25.2
149890	16 36 26.0	30 56 30	51.55	41.19	7.11	25.93	F8V	11	-1	11	± 7	178.4	± 15.5
150433	16 41 08.2	-02 51 26	13.95	27.12	7.22	32.83	G5V	-13	12	18	± 8	68.5	± 12.5
151192	16 46 34.3	-17 35 43	1.70	17.57	8.23	27.56	G5V	36	-10	38	± 10	172.6	± 7.7
151504	16 48 32.2	-19 17 16	0.58	16.18	8.09	26.05	G9IV-V	62	-17	64	± 15	172.5	± 6.6
153631	17 01 10.8	-13 34 02	7.28	17.06	7.14	20.33	G0V	84	0	84	± 9	0.1	± 2.9
155060	17 07 55.8	32 06 20	54.71	34.85	7.22	27.31	F8V	-3	-3	4	± 6	117.1	± 27.5
157172	17 22 34.6	-19 36 58	5.06	9.43	7.86	30.27	G8.5V	32	-22	39	± 15	163.0	± 10.3
164595	18 00 38.9	29 34 19	55.47	23.28	7.07	35.36	G2V	-1	17	17	± 12	46.6	± 17.4
164651	18 02 17.9	00 06 15	27.36	10.96	7.59	30.52	G8V	23	46	51	± 12	31.5	± 6.5
168874	18 20 49.2	27 31 49	55.07	18.41	7.00	34.44	G2IV	55	69	88	± 11	25.6	± 3.6
176377	18 58 51.0	30 10 50	60.97	11.79	6.77	41.72	G1V	-27	36	45	± 8	63.2	± 4.8
180409	19 16 52.2	-10 58 18	25.93	-10.58	6.92	32.52	F9V	-29	4	29	± 7	85.6	± 7.2
190412	20 04 46.6	01 09 22	42.58	-15.71	7.69	29.60	G6/8V	-19	-17	25	± 12	111.3	± 12.8
193017	20 18 10.0	-04 43 43	38.76	-21.43	7.26	25.02	F6V	-33	2	33	± 9	88.5	± 7.9
195034	20 28 11.8	22 07 44	63.96	-9.56	7.10	35.51	G5V	-38	-43	58	± 9	114.3	± 4.5
197210	20 42 29.4	-05 18 05	41.28	-27.06	7.61	33.50	G5V	-31	40	51	± 11	63.9	± 6.0
198075	20 48 15.2	-12 27 16	34.63	-31.49	8.03	24.04	G0.5V	-5	-14	15	± 16	126.0	± 22.9

Table 6. continued.

HD	R.A.	Dec	$l(°)$	$b(°)$	V_{mag}	Par.	Sp	q	u	p	$\pm e_p$	$\theta(°)$	$\pm e_\theta(°)$
202108	21 12 57.6	30 48 34	77.20	-12.07	7.33	36.74	G3V	2	-12	13	± 8	140.2	± 15.7
207966	21 51 52.9	42 20 38	91.04	-9.14	7.86	33.62	G8+M1	-8	-3	8	± 8	101.7	± 22.8
211476	22 17 15.1	12 53 55	74.90	-35.22	7.04	32.69	G2D	-10	-13	16	± 7	116.2	± 10.8
215500	22 44 05.8	64 34 14	109.79	5.00	7.50	39.79	G8V	-5	8	10	± 9	59.9	± 21.8
216275	22 50 46.3	52 03 41	104.81	-6.51	7.15	30.87	G0V	-29	-34	44	± 5	114.6	± 2.5
217924	23 03 50.6	21 35 54	92.13	-34.76	7.22	35.38	G0V	2	-13	13	± 16	139.7	± 25.5
222422	23 40 37.9	-18 59 20	55.78	-71.82	7.58	38.05	G5V	6	-31	31	± 11	140.5	± 9.6
224156	23 55 32.4	03 30 05	97.01	-56.53	7.71	32.59	G6V	-6	-6	9	± 8	112.9	± 20.6

Table 7. Broad-band (400-800 nm) polarimetric data of nearby stars observed at the T60 telescope. The normalized Stokes parameters, q and u, and the degree of polarization, p, are given in units of 10^{-6} (ppm), and the position angle θ in the Equatorial frame of references.

HD	R.A.	Decl.	$l(°)$	$b(°)$	V_{mag}	Par.	Sp	q	u	p	$\pm e_p$	$\theta(°)$	$\pm e_\theta(°)$
123	00 06 15.8	58 26 12	117.03	-3.92	5.98	46.56	G5V	19	6	20	± 9	8.3	± 12.6
203	00 06 50.1	-23 06 27	52.21	-79.14	5.74	25.39	F3V	-4	1	4	± 9	82.1	± 32.0
693	00 11 15.9	-15 28 05	82.23	-75.07	4.89	53.34	F8V	-12	-10	16	± 3	109.1	± 4.9
1388	00 17 58.9	-13 27 20	91.52	-74.25	6.50	36.74	G0V	-19	14	24	± 12	71.8	± 13.6
3795	00 40 32.8	-23 48 18	85.85	-85.87	6.14	35.13	K0V	-15	23	28	± 9	61.6	± 9.2
4247	00 44 44.4	-22 00 22	106.02	-84.66	5.22	37.39	F3V	-16	1	16	± 7	87.5	± 11.8
4307	00 45 28.7	-12 52 51	117.05	-75.68	6.15	31.13	G0V	7	27	28	± 8	37.9	± 8.0
4628	00 48 23.0	05 16 50	121.51	-57.58	5.74	134.50	K2.5V	-2	3	4	± 8	59.2	± 32.8
4813	00 50 07.6	-10 38 40	121.80	-73.51	5.19	63.48	F7V	-7	8	11	± 5	65.4	± 13.1
5015	00 53 04.2	61 07 26	123.13	-1.75	4.80	53.35	F9V	5	6	8	± 3	23.1	± 11.7
7439	01 14 24.0	-07 55 22	139.80	-70.04	5.13	41.83	F5V	-1	-29	29	± 7	134.4	± 6.5
9562	01 33 42.8	-07 01 31	151.38	-67.53	5.76	33.88	G1V	-5	2	6	± 6	82.4	± 22.4
9826	01 36 47.8	41 24 20	132.00	-20.67	4.10	74.12	F9V	3	19	19	± 7	40.5	± 10.5
10307	01 41 47.1	42 36 48	132.71	-19.30	4.96	76.52	G1V	-3	0	3	± 7	84.5	± 34.7
11007	01 48 41.5	32 41 25	136.65	-28.65	5.79	35.90	F8V	-4	6	7	± 10	63.7	± 28.0
11171	01 49 35.1	-10 41 11	165.48	-68.61	4.68	43.13	F0V	53	-35	63	± 7	163.0	± 3.1
11964	01 57 09.6	-10 14 33	168.58	-67.09	6.42	29.79	G9V	82	9	83	± 10	3.1	± 3.4
12235	02 00 09.2	03 05 49	154.34	-55.53	5.90	29.85	G2IV	-1	12	12	± 12	46.9	± 21.8
12230	02 05 07.4	77 16 53	127.06	15.00	5.27	30.16	F0V	-10	29	30	± 9	55.0	± 8.3
14214	02 18 01.4	01 45 28	162.20	-54.38	5.58	43.47	G1V	5	-12	13	± 9	145.3	± 17.5
14412	02 18 58.5	-25 56 45	214.45	-70.41	6.34	77.92	G8V	-24	-2	24	± 9	92.2	± 10.5
14691	02 22 01.5	-10 46 39	179.79	-63.14	5.42	33.72	F3V	25	-9	26	± 6	169.9	± 5.9
15798	02 32 05.2	-15 14 41	191.12	-63.78	4.75	37.46	F5V	27	3	27	± 8	2.8	± 8.6
16160	02 36 04.9	06 53 12	163.40	-47.59	5.79	138.21	K3V	-2	5	6	± 8	57.0	± 26.6
16538	02 38 18.7	-30 11 39	226.75	-66.41	5.83	28.33	F6V	17	-23	28	± 8	153.3	± 7.9
16673	02 40 12.4	-09 27 10	183.54	-58.84	5.79	45.96	F8V	-14	10	17	± 15	71.5	± 21.0
16895	02 44 12.0	49 13 42	141.17	-9.61	4.11	89.87	F8V	15	11	18	± 5	17.8	± 7.8
17948	02 55 56.9	61 31 16	137.21	2.15	5.58	37.44	F5V	5	25	26	± 8	39.9	± 8.5
18907	03 01 37.6	-28 05 29	222.50	-61.23	5.85	31.25	G9V	-38	8	39	± 9	84.0	± 6.6
18692	02 59 36.2	-25 16 27	216.56	-61.27	5.69	29.90	F4V	-28	-12	31	± 7	101.7	± 6.7
18978	03 02 23.5	-23 37 28	213.54	-60.30	4.09	36.80	A3V	-3	-23	23	± 6	131.3	± 7.6
19373	03 09 4.0	49 36 48	144.60	-7.38	4.05	94.87	G0V	-7	12	13	± 11	60.2	± 19.7
20395	03 16 35.8	-09 09 17	192.19	-51.33	6.14	29.26	F5V	-5	0	5	± 9	90.8	± 30.0
21019	03 23 17.7	-07 47 39	191.81	-49.20	6.20	26.92	G5V	14	-7	16	± 9	166.9	± 14.6
22484	03 36 52.4	00 24 06	185.12	-41.67	4.30	71.62	F9V	-5	8	9	± 3	61.6	± 9.8
23754	03 46 50.9	-23 14 59	217.35	-50.32	4.20	56.73	F5IV	-7	-19	20	± 7	124.7	± 10.2
24546	03 56 36.5	50 41 43	150.20	-2.10	5.28	26.01	F5V	6	18	19	± 8	36.5	± 11.0
24740	03 56 52.1	22 28 41	169.59	-23.16	5.62	69.82	F2IV	0	-17	17	± 8	134.7	± 13.0
25621	04 04 09.8	02 49 37	187.90	-34.76	5.36	28.70	F6V	-1	-9	9	± 5	131.3	± 13.2
25680	04 05 20.3	22 00 32	171.45	-22.10	5.90	59.04	G5V	2	4	4	± 5	30.5	± 25.0
25867	04 07 00.5	29 00 05	166.46	-16.90	5.30	36.23	F1V	6	0	6	± 5	1.3	± 19.4
25945	04 05 37.4	-27 39 07	225.31	-47.18	5.59	22.20	F0IV	-15	-38	41	± 8	124.5	± 5.3
26462	04 11 20.3	05 31 23	186.58	-31.72	5.70	27.04	F4V	18	0	18	± 8	0.5	± 11.4
27819	04 24 05.8	17 26 39	178.29	-21.86	4.80	20.21	A2V	16	12	20	± 12	18.7	± 16.0
28527	04 30 33.6	16 11 38	180.38	-21.45	4.76	23.15	A6IV	1	20	20	± 7	43.6	± 10.1
29391	04 37 36.1	-02 28 25	198.61	-30.66	5.21	33.98	F0IV	2	3	4	± 6	27.4	± 27.3
29645	04 41 50.3	38 16 49	164.66	-5.27	5.99	31.38	F9IV-V	-16	8	18	± 6	77.8	± 8.7
30562	04 48 36.4	-05 40 27	203.40	-29.82	5.77	37.85	G2IV	-4	-11	11	± 7	124.4	± 16.6
30606	04 48 32.5	-16 19 46	214.78	-34.37	5.76	23.85	F8V	-5	-6	8	± 8	116.6	± 23.4
30743	04 49 42.2	-13 46 11	212.08	-33.12	6.26	27.44	F6V	-14	-1	14	± 10	91.5	± 17.9
31295	04 54 53.7	10 09 03	189.35	-20.25	4.65	28.04	A0V	8	-13	15	± 10	151.1	± 16.7
31662	05 01 36.0	61 04 41	148.91	11.57	6.04	28.09	F4V	-9	14	16	± 5	61.2	± 9.1
31675	05 02 50.4	66 49 23	144.19	15.03	6.06	35.43	F6V	6	2	7	± 10	10.3	± 27.5
32147	05 00 49.0	-05 45 13	205.09	-27.18	6.21	114.84	K3V	26	2	26	± 9	2.4	± 9.5
33095	05 07 09.8	-19 23 31	220.10	-31.35	6.44	29.18	G1V	-3	10	11	± 8	52.8	± 18.8
33093	05 07 25.0	-12 29 29	212.76	-28.66	5.96	27.25	G0IV	-5	6	8	± 10	62.7	± 25.5
32923	05 07 27.0	18 38 42	183.84	-12.94	5.00	64.79	G4V	18	6	19	± 6	9.7	± 8.8
33021	05 07 38.3	09 28 18	191.77	-18.00	6.17	36.24	G3V	-11	13	17	± 8	65.4	± 12.7
33256	05 08 43.7	-04 27 22	204.84	-24.83	5.12	39.28	F5V	3	2	4	± 5	12.2	± 26.7

Table 7. continued.

HD	R.A.	Dec	$l(°)$	$b(°)$	V_{mag}	Par.	Sp	q	u	p	$\pm e_p$	$\theta(°)$	$\pm e_\theta(°)$
33608	05 11 19.2	-02 29 27	203.27	-23.33	5.89	81.48	F5V	1	5	5	± 7	41.0	± 26.1
34411	05 19 08.5	40 05 57	167.68	1.54	4.71	79.17	G1.5V	-7	0	7	± 7	91.4	± 22.4
34721	05 18 50.5	-18 07 48	219.89	-28.32	5.96	39.96	G0V	9	12	15	± 18	27.5	± 25.5
33564	05 22 33.5	79 13 52	133.73	22.65	5.08	47.88	F6V	-1	-16	16	± 10	133.3	± 15.7
35681	05 28 00.9	33 45 49	173.91	-0.57	6.51	29.17	F7V	-21	21	30	± 10	67.7	± 9.5
35736	05 25 59.8	-19 41 44	222.23	-27.31	5.82	22.21	F5V	4	0	4	± 8	179.3	± 30.1
37495	05 37 44.6	-28 41 23	232.81	-27.75	5.31	24.30	F5V	-25	12	28	± 7	77.5	± 7.4
38382	05 44 28.4	-20 07 36	224.43	-23.43	6.34	38.05	F8.5V	-17	13	21	± 8	71.6	± 10.3
38529	05 46 34.9	01 10 06	204.32	-13.84	5.94	23.58	G8III/	6	15	16	± 9	34.2	± 15.1
38678	05 46 57.3	-14 49 19	219.40	-20.83	3.53	46.28	A2IV-V	-17	24	29	± 5	63.1	± 4.9
38858	05 48 34.9	-04 05 41	209.38	-15.84	5.97	65.63	G2V	0	5	5	± 8	43.0	± 29.0
40650	06 02 45.1	47 48 34	165.13	12.23	6.49	34.95	F5	6	14	15	± 9	32.8	± 15.6
41330	06 06 08.5	35 23 16	176.58	6.98	6.12	39.19	G0V	7	-5	9	± 8	163.6	± 21.3
43042	06 14 50.9	19 09 23	191.80	0.92	5.20	48.04	F5.5V	15	10	18	± 6	16.7	± 9.2
43318	06 15 34.3	00 30 44	209.28	-8.21	5.65	26.89	F5V	8	27	28	± 12	36.3	± 12.0
43386	06 16 26.6	12 16 20	198.03	-2.03	5.04	51.95	F5V	8	0	8	± 7	179.0	± 20.8
43745	06 17 03.6	-22 42 55	230.05	-17.38	6.04	25.00	F9V	-15	18	23	± 8	65.2	± 10.1
43745	06 17 03.6	-22 42 55	230.05	-17.38	6.04	25.00	F9V	15	-12	19	± 10	160.5	± 13.6
45067	06 25 16.5	00 56 45	210.79	-6.25	5.90	29.79	F9V	1	2	2	± 7	36.1	± 35.7
45588	06 27 11.4	-25 51 23	234.01	-16.47	6.07	33.48	F8IV	0	9	9	± 7	46.3	± 19.5
46588	06 46 14.2	79 33 53	134.60	26.41	5.45	55.95	F7V	7	-33	34	± 8	141.1	± 6.9
48097	06 42 24.3	17 38 43	196.17	6.02	5.21	22.92	A2V	29	7	30	± 7	6.5	± 6.8
48938	06 44 52.0	-27 20 30	237.03	-13.42	6.43	37.18	G0V	4	-7	8	± 10	150.4	± 25.5
49933	06 50 49.8	00 32 27	213.34	-0.38	5.78	33.69	F3V	-1	4	5	± 4	52.6	± 22.1
50692	06 55 18.7	25 22 33	190.42	12.06	5.75	58.00	G0V	6	-9	11	± 6	151.2	± 15.3
50806	06 53 33.9	-28 32 23	238.96	-12.16	6.04	38.91	G5V	11	-4	12	± 7	170.5	± 15.9
51733	06 57 33.9	-24 37 51	235.73	-9.70	5.46	26.36	F3V	1	11	11	± 10	41.7	± 20.4
52711	07 03 30.5	29 20 14	187.44	15.32	5.93	52.27	G0V	5	-1	5	± 9	175.2	± 31.2
55575	07 15 50.1	47 14 24	170.34	23.52	5.58	29.06	F9V	12	7	14	± 9	14.6	± 15.8
58461	07 25 08.3	-13 45 07	228.98	1.05	5.78	28.06	F5V	19	8	21	± 8	11.8	± 10.0
58855	07 29 56.0	49 40 21	168.33	26.35	5.36	49.41	F6V	-16	11	20	± 10	73.0	± 13.9
59380	07 29 25.6	-07 33 04	224.02	4.91	5.85	36.71	F6V	6	-1	6	± 5	177.0	± 20.1
59984	07 32 05.8	-08 52 53	225.51	4.86	5.92	35.82	G0V	22	20	30	± 21	21.6	± 17.8
60111	07 33 11.7	03 17 25	214.76	10.79	5.57	23.07	F2IV-V	-12	-21	24	± 8	119.8	± 9.2
60532	07 34 03.2	-22 17 46	237.50	-1.19	4.39	~60.0	F6IV-V	3	8	9	± 6	36.3	± 16.6
63332	07 51 05.7	54 07 45	163.89	30.25	6.02	33.78	F6V	2	0	2	± 8	178.3	± 36.7
64235	07 52 47.9	-05 25 42	224.94	11.03	5.77	25.18	F5IV	23	40	46	± 7	29.9	± 4.3
64685	07 55 31.4	08 51 46	212.16	18.24	5.80	25.63	F3V	10	-4	10	± 12	169.9	± 24.8
67228	08 07 45.9	21 34 55	200.81	25.99	5.30	42.94	G1IV	3	2	3	± 4	16.3	± 27.1
68146	08 10 39.8	-13 47 57	234.56	10.61	5.54	44.68	F6.5V	-2	3	3	± 7	63.2	± 31.6
68255	08 12 12.8	17 38 52	205.30	25.53	6.17	40.96	G0V	-6	2	6	± 5	78.0	± 20.1
69548	08 20 26.1	57 44 36	159.73	34.43	5.88	30.91	F4V	-18	7	19	± 9	79.7	± 12.3
69830	08 18 23.9	-12 37 56	234.56	12.82	5.95	80.04	G8V	4	-31	32	± 6	138.9	± 5.5
69897	08 20 03.9	27 13 04	195.78	30.47	5.10	54.73	F6V	-5	-1	5	± 4	95.9	± 17.7
70110	08 20 13.0	00 54 34	224.31	19.20	6.18	40.95	G0V	6	28	29	± 8	39.4	± 7.6
70958	08 24 35.0	-03 45 05	227.49	18.74	5.61	37.30	F6V	4	-7	8	± 7	150.4	± 20.2
71148	08 27 36.8	45 39 11	174.50	35.42	6.30	45.71	G1V	-12	-9	16	± 8	108.4	± 14.3
71155	08 25 39.6	-03 54 23	227.78	18.89	3.90	26.66	A0V	5	4	6	± 11	16.8	± 29.6
71196	08 25 19.0	-21 02 45	242.67	9.62	5.99	28.44	F2V	17	6	19	± 10	10.2	± 13.9
75332	08 50 32.2	33 17 06	190.53	38.29	6.21	35.27	F7V	-4	-9	10	± 8	122.3	± 18.3
75528	08 51 01.5	15 21 02	211.81	33.26	6.36	24.74	G1V	5	4	7	± 10	18.2	± 27.9
75732	08 52 35.8	28 19 51	196.80	37.70	5.95	81.03	G8V	-2	-2	3	± 8	109.0	± 34.9
76151	08 54 17.9	-05 26 04	233.21	24.16	6.00	57.52	G2V	-15	12	19	± 9	70.8	± 13.0
76932	08 58 43.9	-16 07 58	243.30	18.91	5.86	47.54	G2V	18	17	25	± 14	22.1	± 14.6
78154	09 10 23.5	67 08 03	146.88	38.11	4.80	49.07	F7V	-3	4	5	± 13	63.4	± 34.5
78209	09 08 52.3	51 36 17	166.57	42.02	4.48	34.70	A3V	-13	-5	13	± 5	100.1	± 10.2
78366	09 08 51.1	33 52 56	190.53	42.16	5.90	52.11	G0V	-1	-13	13	± 5	132.8	± 11.5
79028	09 14 20.5	61 25 24	153.62	40.47	5.20	51.10	G0V	19	-2	19	± 7	177.5	± 10.7
80290	09 20 43.8	51 15 58	166.60	43.89	6.11	36.43	F3V	-2	11	11	± 7	49.3	± 17.2
81809	09 27 46.8	-06 04 16	239.14	30.65	5.40	32.88	G1.5V	3	-15	15	± 10	140.9	± 16.4

Table 7. continued.

HD	R.A.	Dec	$l(°)$	$b(°)$	V_{mag}	Par.	Sp	q	u	p	$\pm e_p$	$\theta(°)$	$\pm e_\theta(°)$
81858	09 28 27.4	09 03 24	223.66	38.90	5.41	30.15	G1V	7	-5	9	± 8	161.8	± 20.1
81997	09 29 08.9	-02 46 08	236.23	32.86	4.60	57.69	F5V	8	32	33	± 8	38.2	± 6.8
83287	09 38 21.8	40 14 23	181.86	48.31	5.28	25.88	F0V	-11	-20	22	± 12	120.3	± 14.0
83683	09 40 35.2	13 03 14	220.67	43.34	6.94	24.68	F8V	-202	-567	602	± 11	125.2	± 0.5
84117	09 42 14.4	-23 54 56	256.70	21.52	4.94	66.61	F9V	14	3	14	± 6	5.6	± 11.2
84737	09 48 35.4	46 01 16	172.78	49.43	5.10	54.44	G0.5V	-3	-7	8	± 4	122.6	± 13.7
85376	09 51 53.0	24 23 43	206.42	49.69	5.31	28.45	A5IV	-8	13	15	± 11	60.0	± 17.9
86146	09 57 41.1	41 03 20	180.08	51.89	5.10	35.53	F6V	2	3	4	± 8	27.6	± 31.6
86147	09 56 48.6	04 14 32	233.85	42.52	6.71	22.00	F5/6V	14	9	17	± 11	16.3	± 16.2
86728	10 01 00.7	31 55 25	195.02	52.85	5.40	66.46	G3V	-5	-16	16	± 5	126.2	± 8.4
87301	10 04 08.4	03 12 04	236.44	43.44	6.43	17.85	F3V	20	-14	24	± 8	162.3	± 9.1
87696	10 07 25.8	35 14 41	189.47	54.26	4.49	35.41	A7V	-1	4	5	± 8	54.5	± 30.1
88215	10 10 05.9	-12 48 57	253.29	34.08	5.30	35.95	F3V	-5	6	8	± 8	66.5	± 22.5
89010	10 16 32.3	23 30 11	210.07	54.94	5.97	32.08	G1.5V	2	-3	4	± 14	149.9	± 37.5
89449	10 19 44.2	19 28 15	217.12	54.48	4.80	46.80	F6IV	-2	-18	18	± 8	131.9	± 12.0
89744	10 22 10.6	41 13 46	178.39	56.39	5.72	25.36	F7V	3	3	4	± 9	18.4	± 32.5
90839	10 30 37.6	55 58 50	154.29	51.70	4.82	78.25	F8V	2	-6	6	± 6	144.7	± 20.9
91480	10 35 09.7	57 04 58	152.26	51.57	5.15	37.70	F1V	11	-3	12	± 4	171.9	± 9.5
91889	10 36 32.4	-12 13 48	258.79	38.82	5.70	39.88	F8V	-43	35	55	± 8	70.4	± 4.4
92588	10 41 24.2	-01 44 29	250.38	47.42	6.25	26.52	G9IV	46	7	46	± 9	4.6	± 5.5
92787	10 43 32.9	46 12 14	167.30	58.39	5.18	27.21	F5III	6	0	6	± 5	1.4	± 22.3
95128	10 59 28.0	40 25 49	175.78	63.37	5.04	71.11	G1V	3	-9	10	± 5	144.6	± 13.4
96097	11 05 01.0	07 20 10	246.14	57.94	4.62	34.49	F2III	10	1	10	± 7	4.1	± 16.3
100203	11 32 20.7	61 04 57	138.90	53.52	5.48	35.73	F8V	-8	-15	17	± 10	121.2	± 15.3
100563	11 34 21.9	03 03 37	262.17	59.69	5.70	36.73	F5.5V	10	22	24	± 9	32.9	± 10.1
101198	11 38 40.0	-13 12 07	277.00	45.97	5.48	37.41	F6.5V	-21	22	30	± 7	66.8	± 6.8
102124	11 45 17.0	08 15 29	260.18	65.48	4.84	26.73	A4V	4	8	9	± 5	32.0	± 13.7
104304	12 00 44.5	-10 26 46	283.12	50.47	5.55	78.35	G8IV	-33	-3	33	± 7	92.3	± 5.9
105452	12 08 24.8	-24 43 44	290.66	37.12	4.00	66.95	F1V	-18	5	19	± 9	81.6	± 12.2
106516	12 15 10.6	-10 18 45	288.50	51.54	6.11	44.74	F9V	-9	-29	30	± 12	126.9	± 10.4
108799	12 30 04.8	-13 23 36	294.98	49.15	6.37	40.57	G1/2V	-8	-5	9	± 8	107.5	± 20.9
108954	12 30 50.1	53 04 36	129.94	63.77	6.21	44.72	F9V	15	-8	17	± 9	166.0	± 13.7
109141	12 32 36.0	-13 51 33	295.99	48.76	5.73	26.17	F2V	-17	-19	25	± 10	114.0	± 10.9
110897	12 44 59.4	39 16 44	128.83	77.78	5.95	57.55	F9V	9	-6	10	± 6	163.5	± 14.1
111456	12 48 39.5	60 19 11	123.56	56.81	5.83	41.59	F6V	11	11	16	± 17	22.7	± 23.1
114378	13 09 59.3	17 31 46	327.93	79.49	4.85	~50.0	F5V	-1	-1	2	± 8	104.0	± 39.7
115383	13 16 46.5	09 25 27	322.79	71.31	5.22	56.95	G0V	10	5	11	± 18	13.3	± 29.3
115617	13 18 24.3	-18 18 40	311.86	44.09	4.74	116.89	G6.5V	23	5	24	± 8	6.7	± 9.5
116568	13 24 33.2	-005 9 50	318.09	56.73	5.75	33.37	K2V	-7	21	22	± 7	53.7	± 8.9
117176	13 28 25.8	13 46 44	337.67	74.10	4.97	55.60	G4V	1	-2	2	± 10	148.3	± 39.9
124570	14 14 05.2	12 57 34	0.77	66.03	5.50	29.48	F8V	-18	3	18	± 25	85.0	± 26.8
125451	14 19 16.3	13 00 16	2.76	65.08	5.40	38.32	F5IV	1	-1	1	± 5	164.4	± 37.8
126053	14 23 15.3	01 14 30	347.16	56.02	6.27	57.34	G1.5V	-17	2	17	± 13	86.7	± 18.4
126660	14 25 11.8	51 51 03	93.83	59.65	4.05	68.82	F7V	15	10	18	± 7	17.2	± 10.6
127821	14 30 46.1	63 11 09	105.62	50.47	6.09	31.46	F4IV	-9	0	9	± 10	91.5	± 23.5
132052	14 57 11.0	-04 20 47	351.72	46.27	4.49	37.17	F2V	-9	6	11	± 14	73.6	± 26.2
132254	14 56 23.0	49 37 42	84.64	57.17	5.60	39.83	F8V	10	1	10	± 8	2.0	± 18.8
136064	15 14 38.3	67 20 48	104.57	44.33	5.10	39.46	F8V	-6	4	7	± 7	74.0	± 22.1
137107	15 23 12.2	30 17 18	47.54	56.73	5.58	59.80	G2V	-20	-35	41	± 8	120.1	± 5.3
137898	15 28 38.2	01 50 32	5.82	44.67	5.17	25.16	A6III	-13	-36	38	± 6	124.9	± 4.3
140583	15 44 01.8	02 30 55	9.70	41.97	5.86	67.71	G2.5V	-13	16	20	± 7	64.2	± 9.3
142373	15 52 40.5	42 27 06	67.70	50.32	4.62	62.92	F8V	3	0	3	± 6	0.9	± 32.1
143761	16 01 02.7	33 18 13	53.49	48.92	5.42	57.22	G0V	18	8	20	± 6	12.0	± 8.0
147365	16 19 55.1	39 42 31	63.12	45.37	5.48	37.91	F4V	31	9	32	± 7	8.5	± 6.0
147449	16 22 04.3	01 01 45	14.78	33.23	4.82	36.67	A9II	14	1	14	± 7	1.2	± 12.7
152598	16 52 58.1	31 42 06	53.39	37.87	5.33	34.26	F0V	2	1	2	± 6	8.3	± 35.8
154905	17 05 20.2	54 28 14	82.30	37.02	5.69	36.80	F6V	-9	18	20	± 11	59.2	± 14.1
159332	17 33 22.8	19 15 24	42.48	25.53	5.65	25.87	F4V	-8	-8	11	± 7	112.4	± 16.5
160915	17 43 25.8	-21 40 60	5.93	4.21	4.86	56.65	F5V	7	-1	7	± 7	177.8	± 23.1
162917	17 53 14.2	06 06 05	31.78	15.71	5.76	32.47	F4IV/V	49	16	51	± 11	9.0	± 6.1

Table 7. continued.

HD	R.A.	Dec	$l(°)$	$b(°)$	V_{mag}	Par.	Sp	q	u	p	$\pm e_p$	$\theta(°)$	$\pm e_\theta(°)$
164259	18 00 29.0	-03 41 25	23.73	9.58	4.62	42.46	F2V	4	15	16	± 17	37.6	± 23.9
173667	18 45 39.7	20 32 47	50.79	10.43	4.19	52.06	F6V	-37	-1	37	± 8	90.5	± 5.9
184960	19 34 19.8	51 14 12	83.46	14.59	5.73	39.45	F7V	-8	8	11	± 10	67.9	± 20.0
185124	19 37 47.3	-04 38 52	34.06	-12.42	5.68	31.17	F3IV/V	-18	2	18	± 8	87.3	± 11.9
185395	19 36 26.5	50 13 16	82.67	13.85	4.48	54.54	F3V	3	35	35	± 8	42.3	± 6.6
187013	19 46 25.6	33 43 39	68.81	4.43	4.99	47.10	F5.5V	9	-13	16	± 11	152.6	± 17.2
187691	19 51 01.6	10 24 57	49.14	-8.20	5.10	52.11	F8V	-3	11	11	± 16	51.7	± 27.9
190406	20 04 06.2	17 04 13	56.28	-7.55	5.80	56.28	G0V	-4	-4	5	± 5	112.9	± 22.1
191195	20 06 13.8	53 09 57	87.56	11.18	5.85	27.35	F5V	-40	13	42	± 10	80.7	± 7.0
193664	20 17 31.3	66 51 13	100.46	16.91	5.93	56.92	G3V	27	-5	28	± 12	174.9	± 11.4
200790	21 05 26.7	05 57 30	55.38	-26.18	5.94	26.25	F8V	-2	-6	7	± 8	126.7	± 25.7
205289	21 34 51.1	-20 05 03	30.88	-44.70	5.70	36.90	F5V	-3	0	3	± 15	93.1	± 38.8
206826	21 44 08.6	28 44 33	80.59	-18.34	4.51	42.10	F7V	-14	-9	17	± 9	106.1	± 14.4
207958	21 53 17.8	-13 33 06	41.89	-46.35	5.08	37.57	F2V	-6	-2	7	± 7	99.0	± 24.2
209369	21 59 15.0	73 10 48	111.17	14.38	5.04	27.23	F5V	9	1	9	± 7	1.8	± 19.6
210855	22 11 48.2	59 43 15	102.39	0.48	5.20	26.77	F8V	7	-6	9	± 6	160.6	± 17.2
212697	22 26 34.3	-16 44 30	42.55	-54.98	6.32	49.80	G3V	-18	-10	20	± 9	104.7	± 11.7
213845	22 34 41.6	-20 42 30	37.08	-58.20	5.20	44.09	F7V	-6	-12	13	± 5	121.9	± 10.9
215648	22 46 41.6	12 10 22	81.28	-40.40	4.10	61.36	F6V	-7	-8	11	± 7	115.1	± 15.9
216385	22 52 24.1	09 50 08	80.87	-43.11	5.18	37.13	F6V	-17	-2	17	± 5	93.4	± 8.7
218470	23 07 45.4	49 17 45	106.10	-10.16	5.70	29.12	F5V	-3	-1	3	± 7	99.8	± 34.9
218804	23 10 27.2	43 32 38	104.21	-15.63	5.93	34.10	F5V	-12	-3	12	± 9	96.1	± 19.0
219080	23 12 33.0	49 24 22	106.87	-10.35	4.52	40.67	F1V	-5	-13	14	± 5	123.4	± 9.2
219623	23 16 42.3	53 12 49	108.93	-7.06	5.60	48.77	F7V	4	15	16	± 8	37.3	± 12.6
219877	23 19 24.0	-05 07 28	73.94	-58.94	5.56	28.94	F4V	6	-4	7	± 9	163.3	± 26.0
225003	00 02 29.7	08 29 08	102.81	-52.46	5.69	27.10	F1V	-1	-5	5	± 6	130.8	± 24.4

Table 11. Stars showing evidence of polarization variability from the observations at the T60 telescope. The normalized Stokes parameters, q and u, and the degree of polarization, p, are given in units of 10^{-6} (ppm) for stars showing observed standard deviation of q and u > twice the value expected from the errors of the nightly points.

HD	q	u	$p \pm e_p$	$\theta \pm e_\theta(^\circ)$	J.D.
16673	-21	31	37 ± 9	61.7 ± 7.0	8092.8290
16673	-8	-6	10 ± 8	107.7 ± 19.1	8428.9127
av.	-14	10	17 ± 15	71.5 ± 21.0	
19373	-9	5	10 ± 4	75.2 ± 11.3	7041.7720
19373	0	7	7 ± 7	43.0 ± 22.2	7299.0752
19373	-3	12	12 ± 9	51.6 ± 19.0	7777.7679
19373	-10	44	45 ± 8	51.5 ± 4.9	8027.1158
av.	-7	12	13 ± 11	60.2 ± 19.7	
34411	0	-3	3 ± 6	134.3 ± 32.5	7042.8518
34411	11	13	17 ± 12	24.6 ± 17.9	7776.7704
34411	-17	14	22 ± 5	71.0 ± 6.6	8029.1594
34411	0	-19	19 ± 6	134.1 ± 8.7	8141.8296
34411	-10	-3	11 ± 6	99.4 ± 14.5	8415.0332
av.	-7	0	7 ± 7	91.4 ± 22.4	
34721	22	27	34 ± 7	25.4 ± 5.9	7359.0229
34721	-9	-7	11 ± 8	108.9 ± 17.6	7689.1105
av.	9	12	15 ± 18	27.5 ± 25.5	
43042	-3	-6	6 ± 7	123.3 ± 22.8	7045.9026
43042	12	16	20 ± 9	26.3 ± 12.2	7778.8921
43042	11	8	13 ± 6	17.6 ± 12.3	8054.0775
43042	30	19	36 ± 6	16.2 ± 5.1	8134.9385
43042	18	11	21 ± 7	16.2 ± 9.5	8425.0300
av.	15	10	18 ± 6	16.7 ± 9.2	
43386	0	0	1 ± 6	147.6 ± 40.0	7040.9517
43386	13	13	18 ± 7	22.2 ± 10.8	7690.7510
43386	8	-27	28 ± 7	143.4 ± 6.6	8046.0954
43386	0	15	15 ± 7	45.1 ± 12.1	8137.9264
43386	20	0	20 ± 7	178.7 ± 9.3	8424.0413
av.	8	0	8 ± 7	179.0 ± 20.8	
55575	-6	4	7 ± 8	74.2 ± 23.7	7039.9816
55575	39	-16	42 ± 9	169.0 ± 5.8	7357.7496
55575	18	17	25 ± 7	21.5 ± 8.2	7777.8440
55575	5	13	14 ± 7	33.9 ± 13.7	8065.0556
av.	12	7	14 ± 9	14.6 ± 15.8	
58855	-10	-1	10 ± 5	96.6 ± 13.7	7043.9796
58855	-10	40	41 ± 5	52.1 ± 3.5	7355.6213
58855	-31	6	32 ± 7	84.8 ± 6.5	7492.6318
58855	-29	-5	29 ± 7	94.7 ± 7.1	7780.9514
58855	-9	-11	14 ± 10	116.1 ± 17.4	8045.1089
av.	-16	11	20 ± 10	73.0 ± 13.9	
59984	-16	-11	19 ± 11	107.7 ± 15.3	7359.1496
59984	21	12	24 ± 10	15.3 ± 11.3	7494.6338
59984	37	37	52 ± 7	22.6 ± 3.8	8090.5173
av.	22	20	30 ± 21	21.6 ± 17.8	
83287	-8	-3	9 ± 6	101.9 ± 17.3	7040.0560
83287	-14	-36	39 ± 6	124.1 ± 4.6	8489.9996
av.	-11	-20	22 ± 12	120.3 ± 14.0	
89449	0	-9	9 ± 8	134.0 ± 21.4	7777.9931
89449	2	-30	30 ± 6	137.0 ± 5.9	8068.0886
89449	-11	-7	13 ± 8	105.5 ± 16.1	8195.8679
av.	-2	-18	18 ± 8	131.9 ± 12.0	
115383	0	-19	19 ± 9	135.5 ± 12.1	7786.1496
115383	18	24	30 ± 8	26.3 ± 7.6	7895.7726
av.	10	5	11 ± 18	13.3 ± 29.3	

Table 11. continued.

HD	q	u	$p \pm e_p$	$\theta \pm e_\theta(^\circ)$	J.D.
164259	-3	14	15 ± 7	51.7 ± 13.0	7165.0349
164259	28	19	34 ± 13	17.2 ± 10.1	8025.7328
av.	4	15	16 ± 17	37.6 ± 23.9	
187691	-8	0	8 ± 6	92.1 ± 19.0	7688.7194
187691	7	32	33 ± 8	38.5 ± 6.9	8320.0818
av.	-3	11	11 ± 16	51.7 ± 27.9	
205289	5	20	20 ± 8	37.8 ± 10.5	7246.9797
205289	6	-23	24 ± 8	142.6 ± 9.5	7687.7755
205289	-36	4	37 ± 11	87.0 ± 8.6	8334.0697
av.	-3	0	3 ± 15	93.1 ± 38.8	
206826	-6	-3	7 ± 5	101.3 ± 17.1	7242.9986
206826	-29	-5	30 ± 7	94.8 ± 6.9	7355.7187
206826	-16	-25	30 ± 7	118.7 ± 6.4	8029.2428
av.	-14	-9	17 ± 9	106.1 ± 14.4	
207958	1	16	16 ± 7	43.5 ± 12.5	7245.9160
207958	-5	-14	15 ± 8	125.5 ± 14.5	7297.8723
207958	-27	-15	31 ± 7	104.4 ± 6.7	7357.7294
207958	-23	10	26 ± 9	78.0 ± 9.4	7687.7141
207958	-9	-8	12 ± 8	110.0 ± 16.9	8045.7484
207958	12	0	12 ± 6	178.1 ± 13.7	8336.0769
av.	-6	-2	7 ± 7	99.0 ± 24.2	
215648	-10	-5	11 ± 5	103.9 ± 11.1	6997.2817
215648	-18	-9	20 ± 8	103.8 ± 10.6	7297.9262
215648	-28	-7	29 ± 8	96.6 ± 8.1	7353.7497
215648	-3	-24	24 ± 7	131.8 ± 7.8	7694.7977
215648	7	-16	17 ± 9	146.5 ± 13.7	8044.7735
215648	7	2	8 ± 6	8.9 ± 20.2	8316.0982
av.	-7	-8	11 ± 7	115.1 ± 15.9	